12. MEMS/NEMS Devices and Applications

MEMS/NEMS

Darrin J. Young, Christian A. Zorman, Mehran Mehregany

Microelectromechanical systems (MEMS) have played key roles in many important areas, for example transportation, communication, automated manufacturing, environmental monitoring, health care, defense systems, and a wide range of consumer products. MEMS are inherently small, thus offering attractive characteristics such as reduced size, weight, and power dissipation and improved speed and precision compared to their macroscopic counterparts. Integrated circuit (IC) fabrication technology has been the primary enabling technology for MEMS besides a few special etching, bonding and assembly techniques. Microfabrication provides a powerful tool for batch processing and miniaturizing electromechanical devices and systems to a dimensional scale that is not accessible by conventional machining techniques. As IC fabrication technology continues to scale toward deep submicrometer and nanometer feature sizes, a variety of nanoelectromechanical systems (NEMS) can be envisioned in the foreseeable future. Nanoscale mechanical devices and systems integrated with nanoelectronics will open a vast number of new exploratory research areas in science and engineering. NEMS will most likely serve as an enabling technology, merging engineering with the life sciences in ways that are not currently feasible with microscale tools and technologies.

MEMS has been applied to a wide range of fields. Hundreds of microdevices have been developed for specific applications. It is thus difficult to provide an overview covering every aspect of the topic. In this chapter, key aspects of MEMS technology and applications are illustrated by selecting a few demonstrative device examples, such as pressure sensors, inertial sensors, optical and wireless communication devices. Microstructure examples with dimensions on the order of submicrometer are presented with fabrication technologies for future NEMS applications.

Although MEMS has experienced significant growth over the past decade, many challenges still remain. In broad terms, these challenges can be grouped into three general categories: (1) fabrication challenges; (2) packaging challenges; and (3) application challenges. Challenges in these areas will, in large measure, determine the commercial success of a particular MEMS device in both technical and economic terms. This chapter presents a brief discussion of some of these challenges as well as possible approaches to addressing them.

Microelectromechanical Systems, generally referred to as MEMS, has had a history of research and development over a few decades. Besides the traditional microfabricated sensors and actuators, the field covers micromechanical components and systems integrated or microassembled with electronics on the same substrate or package, achieving high-performance functional systems. These devices and systems have played key roles in many important areas such as transportation, communication, automated manufacturing, environmental

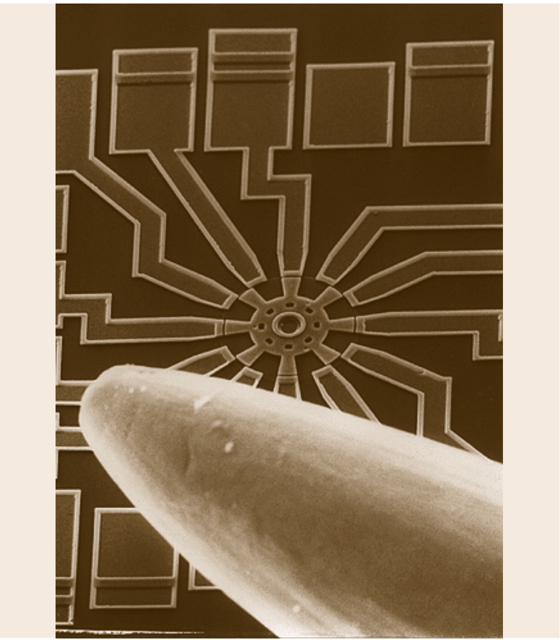

Fig. 12.1 SEM micrograph of a polysilicon microelectromechanical motor (after [12.1])

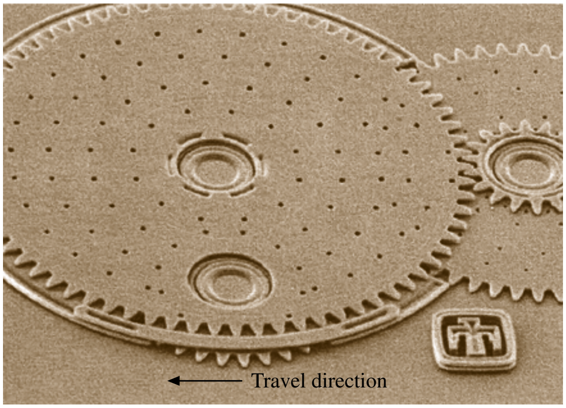

Fig. 12.2 SEM micrograph of polysilicon microgears (after [12.3])

monitoring, health care, defense systems, and a wide range of consumer products. MEMS are inherently small, thus offering attractive characteristics such as reduced size, weight, and power dissipation and improved speed and precision compared to their macroscopic counterparts. The development of MEMS requires appropriate fabrication technologies that enable the definition of small geometries, precise dimension control, design flexibility, interfacing with microelectronics, repeatability, reliability, high yield, and low cost. Integrated circuits (IC) fabrication technology meets all of the above criteria and has been the primary enabling fabrication technology for MEMS besides a few special etching, bonding and assembly techniques. Microfabrication provides a powerful tool for batch processing and miniaturization of electromechanical devices and systems into a dimensional scale, which is not accessible by conventional machining techniques. Most MEMS devices exhibit a length or width ranging from micrometers to several hundreds of micrometers with a thickness from submicrometer up to tens of micrometers depending upon fabrication technique employed. A physical displacement of a sensor or an actuator is typically on the same order of magnitude. Figure 12.1 shows an SEM micrograph of a microelectromechanical motor developed in late 1980s [12.1]. Polycrystalline silicon (polysilicon) surface micromachining technology was used to fabricate the micromotor achieving a diameter of 150 μm and a minimum vertical feature size on the order of a micrometer. A probe tip is also shown in the micrograph for a size comparison. This device example and similar others [12.2] demonstrated at that time what MEMS technology could accomplish in microscale machining and served as a strong technology indicator for continued MEMS development. The field has expanded greatly in recent years along with rapid technology advances. Figure 12.2, for example, shows a photo of microgears fabricated in mid-1990s using a five-level polysilicon surface micromachining technology [12.3]. This device represents one of the most advanced surface micromachining fabrication process developed to date. One can imagine that a wide range of sophisticated microelectromechanical devices and systems can be realized through applying such technology in the future. As IC fabrication technology continues to scale toward deep submicrometer and nanometer feature sizes, a variety of nanoelectromechanical systems (NEMS) can be envisioned in the foreseeable future. Nanoscale mechanical devices and systems integrated with nanoelectronics will open a vast number of new exploratory research areas in science and engineering. NEMS will most likely serve as an enabling technology merging engineering with the life sciences in ways that are not currently feasible with the microscale tools and technologies.

This chapter will provide a general overview on MEMS and NEMS devices along with their applications. MEMS technology has been applied to a wide range of fields. Over hundreds of microdevices have been developed for specific applications. Thus, it is difficult to provide an overview covering every aspect of the topic. It is the authors' intent to illustrate key aspects of MEMS technology and its impact to specific applications by selecting a few demonstrative device examples in this chapter. For a wide-ranging discussion of nearly all types of micromachined sensors and actuators, books by *Kovacs* [12.4] and *Senturia* [12.5] are recommended.

12.1 MEMS Devices and Applications

MEMS devices have played key roles in many areas of development. Microfabricated sensors, actuators, and electronics are the most critical components required to implement a complete system for a specific function. Microsensors and actuators can be fabricated by various micromachining processing technologies. In this section, a number of selected MEMS devices are presented to illustrate the basic device operating principles as well as to demonstrate key aspects of the microfabrication technology and application impact.

12.1.1 Pressure Sensor

Pressure sensors are one of the early devices realized by silicon micromachining technologies and have become successful commercial products. The devices have been widely used in various industrial and biomedical applications. The sensors can be based on piezoelectric, piezoresistive, capacitive, and resonant sensing mechanisms. Silicon bulk and surface micromachining techniques have been used for sensor batch fabrication, thus achieving size miniaturization and low cost. Two types of pressure sensors, piezoresistive and capacitive, are described here for an illustration purpose.

Piezoresistive Sensor

The piezoresisitve effect in silicon has been widely used for implementing pressure sensors. A pressure-induced strain deforms the silicon band structure, thus changing the resistivity of the material. The piezoresistive effect is typically crystal orientation dependent and is also affected by doping and temperature. A practical piezoresistive pressure sensor can be implemented by fabricating four sensing resistors along the edges of a thin silicon diaphragm, which acts as a mechanical amplifier to increase the stress and strain at the sensor site. The four sensing elements are connected in a bridge configuration with push–pull signals to increase the sensitivity. The measurable pressure range for such a sensor can be from 10^{-3} to 10^{6} Torr depending upon the design. An example of a piezoresistive pressure sensor is shown in Fig. 12.3. The device consists of a silicon diaphragm suspended over a reference vacuum cavity to form an absolute pressure sensor. An external pressure applied over the diaphragm introduces a stress on the sensing resistors, thus resulting in a resistance value change corresponding to the pressure. The fabrication sequence is outlined as follows. The piezoresistors are typically first formed through a boron diffusion process followed by a high-temperature annealing step in order to achieve a resistance value on the order of a few kiloohms. The wafer is then passivated with a silicon dioxide layer and contact windows are opened for metallization. At this point, the wafer is patterned on the backside, followed by a timed silicon wet etch to form the diaphragm, typically having a thickness around a few tens of micrometers. The diaphragm can have a length of several hundreds of micrometers. A second silicon wafer is then bonded to the device wafer in vacuum to form a reference vacuum cavity, thus completing the fabrication process. The second wafer can also be further etched through to form an inlet port, implementing a gauge pressure sensor [12.6]. The piezoresistive sensors are simple to fabricate and can be readily interfaced with electronic systems. However, the resistors are temperature dependent and consume DC power. Long-term characteristic drift and resistor thermal noise ultimately limit the sensor resolution.

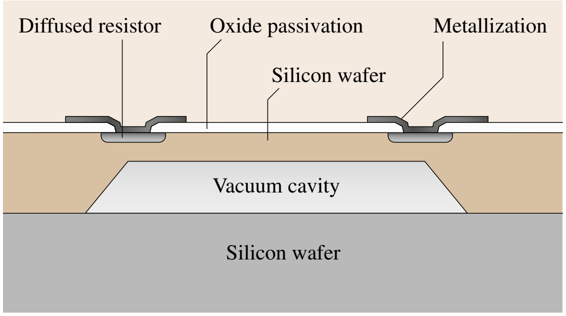

Fig. 12.3 Cross-sectional schematic of a piezoresistive pressure sensor

Capacitive Sensor

Capacitive pressure sensors are attractive because they are virtually temperature independent and consume zero

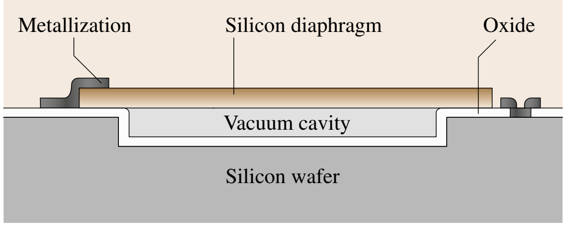

Fig. 12.4 Cross-sectional schematic of a capacitive pressure sensor

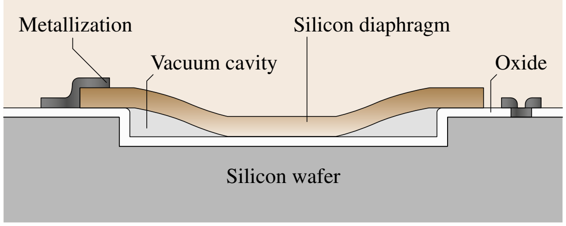

Fig. 12.5 Cross-sectional schematic of a touch-mode capacitive pressure sensor

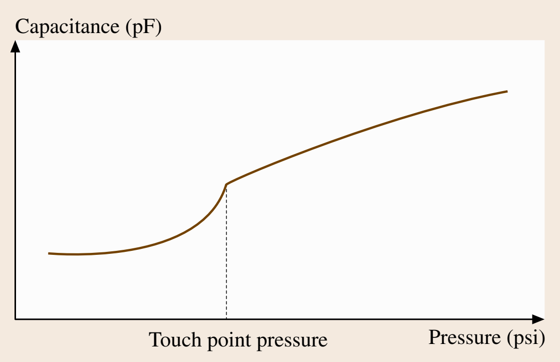

Fig. 12.6 Touch-mode capacitive pressure sensor characteristic response

DC power. The devices do not exhibit initial turn-on drift and are stable over time. Furthermore, CMOS microelectronic circuits can be readily interfaced with the sensors to provide advanced signal conditioning and processing, thus improving overall system performance. An example of a capacitive pressure sensor is shown in Fig. 12.4. The device consists of an edge clamped silicon diaphragm suspended over a vacuum cavity. The diaphragm can be square or circular with a typical thickness of a few micrometers and a length or radius of a few hundreds micrometers, respectively. The vacuum cavity typically has a depth of a few micrometers. The diaphragm and substrate form a pressure dependent air-gap variable capacitor. An increased external pressure causes the diaphragm to deflect towards the substrate, thus resulting in an increase in the capacitance value. A simplified fabrication process can be outlined as follows. A silicon wafer is first patterned and etched to form the cavity. The wafer is then oxidized followed by bonding to a second silicon wafer with a heavily-doped boron layer, which defines the diaphragm thickness, at the surface. The bonding process can be performed in vacuum to realize the vacuum cavity. If the vacuum bonding is not performed at this stage, a low pressure sealing process can be used to form the vacuum cavity after patterning the sensor diaphragm, provided that sealing channels are available. The silicon substrate above the boron layer is then removed through a wet etching process, followed by patterning to form the sensor diaphragm, which serves as the device top electrode. Contact pads are formed by metallization and patterning. This type of pressure sensor exhibits a nonlinear characteristic and a limited dynamic range. These phenomena, however, can be alleviated through applying an electrostatic force-balanced feedback architecture. A common practice is to introduce another electrode above the sensing diaphragm through wafer bonding [12.7], thus forming two capacitors in series with the diaphragm being the middle electrode. The capacitors are interfaced with electronic circuits, which convert the sensor capacitance value to an output voltage corresponding to the diaphragm position. This voltage is further processed to generate a feedback signal to the top electrode, thus introducing an electrostatic pull up force to maintain the deflectable diaphragm at its nominal position. This negative feedback loop would substantially minimize the device nonlinearity and also extend the sensor dynamic range.

A capacitive pressure sensor achieving an inherent linear characteristic response and a wide dynamic range can be implemented by employing a touch-mode architecture [12.8]. Figure 12.5 shows the cross-sectional view of a touch-mode pressure sensor. The device consists of an edge-clamped silicon diaphragm suspended over a vacuum cavity. The diaphragm deflects under an increasing external pressure and touches the substrate, causing a linear increase in the sensor capacitance value beyond the touch point pressure. Figure 12.6 shows a typical device characteristic curve. The touch point pressure can be designed through engineering the sensor geometric parameters such as the diaphragm size, thickness, cavity depth, etc., for various application requirements. The device can be fabricated using a process flow similar to the flow outlined for the basic

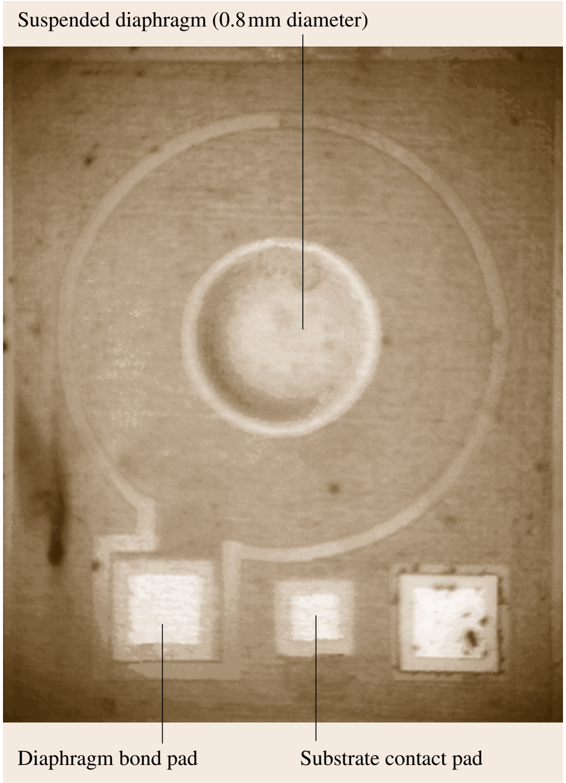

Fig. 12.7 Photo of a touch-mode capacitive pressure sensor (after [12.8])

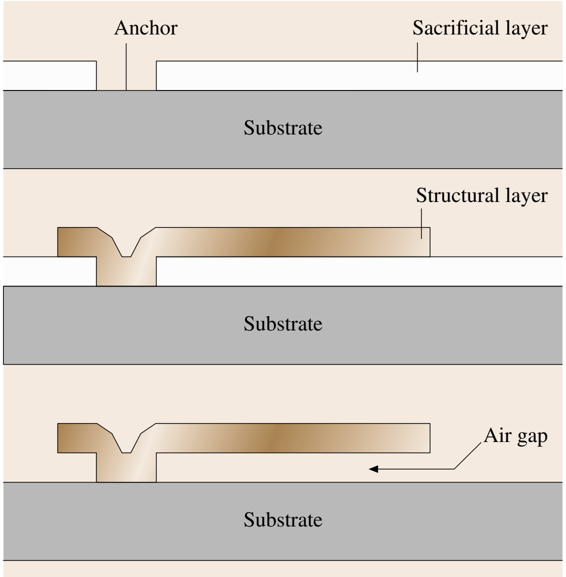

Fig. 12.8 Simplified fabrication sequence of surface micromachining technology

capacitive pressure sensor. Figure 12.7 presents a photo of a fabricated touch-mode sensor employing a circular diaphragm with a diameter of 800 µm and a thickness of 5 µm suspended over a 2.5 µm vacuum cavity. The device achieves a touch point pressure of 8 psi and exhibits a linear capacitance range from 33 pF at 10 psi to 40 pF at 32 psi (absolute pressures). Similar sensor structures have been demonstrated by using single-crystal 3C-SiC diaphragm achieving a high-temperature pressure sensing capability up to 400 °C [12.9].

The above processes use bulk silicon materials for machining and are usually referred to as bulk micromachining. The same devices can also be fabricated using so called surface micromachining. Surface micromachining technology is attractive for integrating MEMS sensors with on-chip electronic circuits. As a result, advanced signal processing capabilities such as data conversion, offset and noise cancellation, digital calibration, temperature compensation, etc. can be implemented adjacent to microsensors on a same substrate, providing a complete high-performance microsystem solution. The single chip approach also eliminates external wiring, which is critical for minimizing noise pick up and enhancing system performance. Surface micromachining, simply stated, is a method of fabricating MEMS through depositing, patterning, and etching a sequence of thin films with thickness on the order of a micrometer. Figure 12.8 illustrates a typical surface micromachining process flow [12.11]. The process

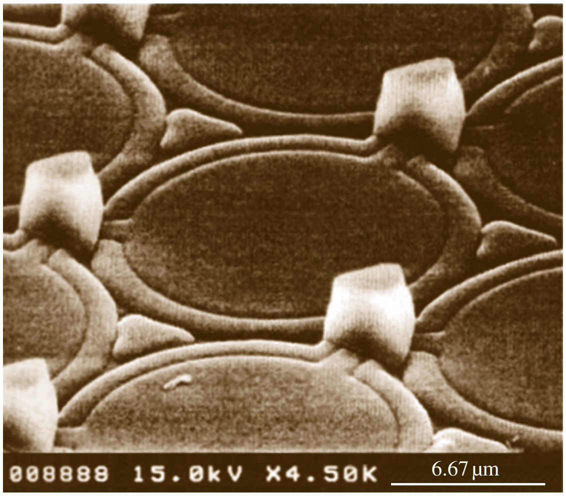

Fig. 12.9 SEM micrograph of polysilicon surface-micromachined capacitive pressure sensors (after [12.10])

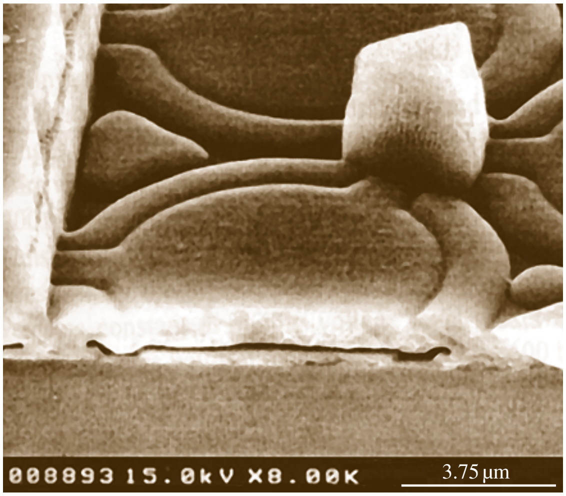

Fig. 12.10 SEM micrograph of a close-up view of a polysilicon surface-micromachined capacitive pressure sensor (after [12.10])

starts by depositing a layer of sacrificial material such as silicon dioxide over a wafer followed by anchor formation. A structural layer, typically a polysilicon film, is deposited and patterned. The underlying sacrificial layer is then removed to freely release the suspended microstructure and to complete the fabrication sequence. The processing materials and steps are compatible with standard integrated circuit process, thus can be readily incorporated as an add-on module to an IC process [12.11–13]. A similar surface micromachining technology has been developed to produce monolithic pressure sensor systems [12.10]. Figure 12.9 shows an SEM micrograph of an array of MEMS capacitive pressure sensors fabricated with BiCMOS electronics on the same substrate. Each sensor consists of a 0.8 µm thick circular polysilicon membrane with a diameter on the order of 20 µm suspended over a 0.3 µm deep vacuum cavity. The devices operate using the same principle as the sensor shown in Fig. 12.4. A close view of the sensor cross-section is shown in Fig. 12.10, which shows the suspended membrane and underneath air gap. These sensors have demonstrated operations in pressure ranges up to 400 bar with an accuracy of 1.5%.

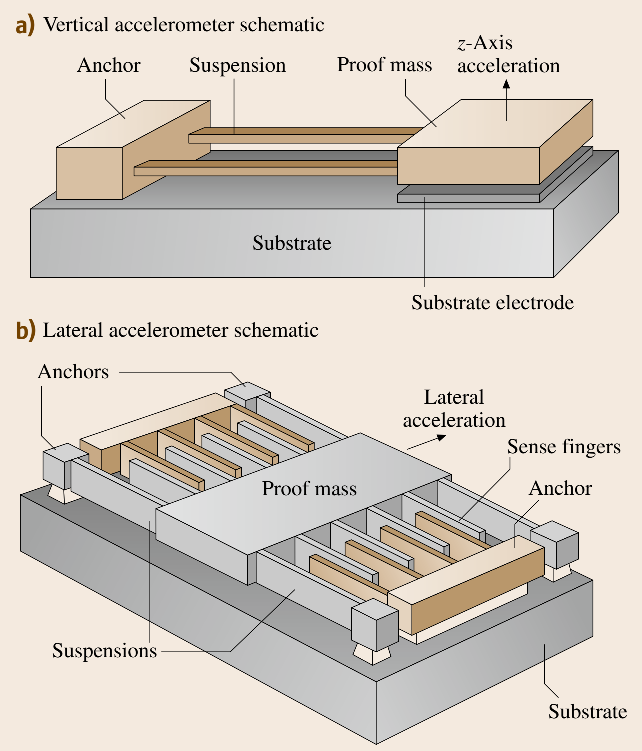

Fig. 12.11a,b Schematics of vertical and lateral accelerometers

12.1.2 Inertial Sensor

Micromachined inertial sensors consist of accelerometers and gyroscopes. These devices are one of the important types of silicon-based MEMS sensors that have been successfully commercialized. MEMS accelerometers alone have the second largest sales volume after pressure sensors. Gyroscopes are expected to reach a comparable sales volume in a foreseeable future. Accelerometers have been used in a wide range of applications including automotive application for safety systems, active suspension and stability control, biomedical application for activity monitoring, and numerous consumer products such as head-mount displays, camcorders, three-dimensional mouse, etc. High-sensitivity accelerometers are crucial for implementing self-contained navigation and guidance systems. A gyroscope is another type of inertial sensor that measures rate or angle of rotation. The devices can be used along with accelerometers to provide heading information in an inertial navigation system. Gyroscopes also are useful in applications such as automotive ride stabilization and rollover detection, camcorder stabilization, virtual reality, etc. Inertial sensors fabricated by micromachining technology can achieve reduced size, weight, and cost, all which are critical for consumer applications. More importantly, these sensors can be integrated with microelectronic circuits to achieve a functional microsystem with high performance.

Accelerometer

An accelerometer generally consists of a proof mass suspended by compliant mechanical suspensions anchored to a fixed frame. An external acceleration displaces the support frame relative to the proof mass. The displacement can result in an internal stress change in the suspension, which can be detected by piezoresistive sensors as a measure of the external acceleration. The displacement can also be detected as a capacitance change in capacitive accelerometers. Capacitive sensors are attractive for various applications because they exhibit high sensitivity and low temperature dependence, turn-on drift, power dissipation, and noise. The sensors can also be readily integrated with CMOS electronics to perform advanced signal processing for high system performance. Capacitive accelerometers may be divided into two categories as vertical and lateral type sensors. Figure 12.11 shows sensor structures for the two versions. In a vertical device, the proof mass is suspended above the substrate electrode by a small gap typically on the order of a micrometer, forming a parallel-plate sense capacitance. The proof mass moves in the direction perpendicular to the substrate (z-axis) upon a vertical input acceleration, thus changing the gap and hence the capacitance value. The lateral accelerometer consists of a number of movable fingers attached to the proof mass, forming a sense capacitance with an array of fixed parallel fingers. The sensor proof mass moves in a plane parallel to the substrate when subjected to a lateral input acceleration, thus changing the overlap area of these fingers; hence the capacitance value. Figure 12.12 shows an SEM top view of a surface-micromachined polysilion z-axis accelerometer [12.14]. The device consists of a $400 \times 400\,\mu\text{m}^2$ proof mass with a thickness of $2\,\mu\text{m}$ suspended above the substrate electrode by four folded beam suspensions with an air gap around $2\,\mu\text{m}$, thus achieving a sense capacitance of $\approx 500\,\text{fF}$. The visible holes are used to ensure complete removal of the sacrificial oxide underneath the proof mass at the end of the fabrication process. The sensor can be interfaced with a microelectronic charge amplifier converting the capacitance value to an output voltage for further signal processing and analysis. Force feedback architecture can be applied to stabilize the proof mass position. The combs around the periphery of the proof mass can exert an electrostatic levitation force on the proof mass to achieve the position control, thus improving the system frequency response and linearity performance [12.14].

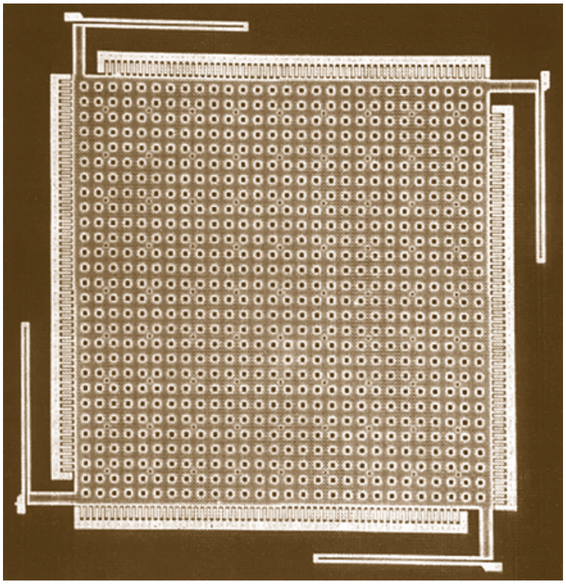

Fig. 12.12 SEM micrograph of a polysilicon surface-micromachined z-axis accelerometer (after [12.14])

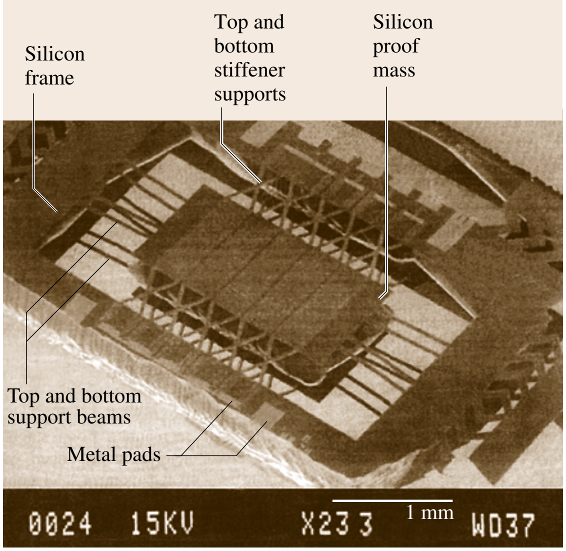

Fig. 12.13 SEM micrograph of a MEMS z-axis accelerometer fabricated by using a combined surface and bulk micromachining technology (after [12.15])

Surface micromachined accelerometers typically suffer from severe mechanical thermal vibration, commonly referred to as Brownian motion [12.16], due to the small proof mass, thus resulting in a high mechanical noise floor which ultimately limits the sensor resolution. Vacuum packaging can be employed to minimize this adverse effect but with a penalty of increasing

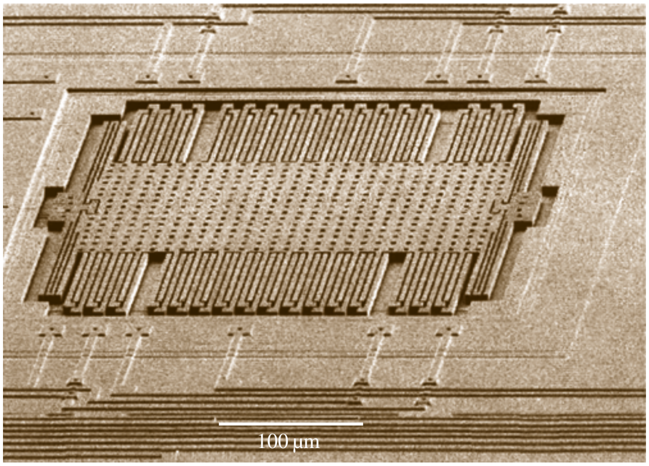

Fig. 12.14 SEM micrograph of a polysilicon surface-micromachined lateral accelerometer (© Analog Devices Inc.)

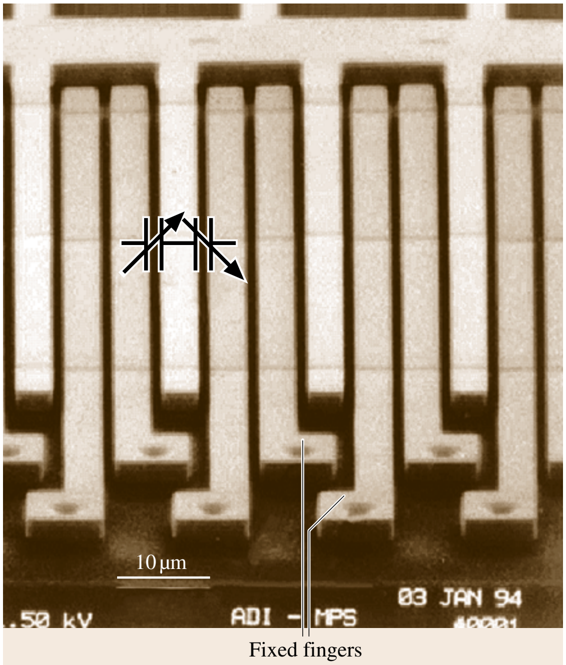

Fig. 12.15 SEM micrograph of a capacitive sensing finger structure

system complexity and cost. Accelerometers using large proof masses fabricated by bulk micromachining or a combination of surface and bulk micromachining techniques are attractive for circumventing this problem. Figure 12.13 shows an SEM micrograph of an all-silicon z-axis accelerometer fabricated through a single silicon wafer by using combined surface and bulk micromachining process to obtain a large proof mass with dimensions of $\approx 2\times1\times450\,\mu\text{m}^3$ [12.15]. The large mass suppresses the Brownian motion effect, achieving a high performance with a resolution on the order of several µg. Similar fabrication techniques have been used to demonstrate a three-axis capacitive accelerometer achieving a noise floor of $\approx 1\,\mu\text{g}/\sqrt{\text{Hz}}$ [12.17].

A surface-micromachined lateral accelerometer developed by Analog Devices Inc. is shown in Fig. 12.14. The sensor consists of a center proof mass supported by folded beam suspensions with arrays of attached movable fingers, forming a sense capacitance with the fixed parallel fingers. The device is fabricated using a 6 µm thick polysilicon structural layer with a small air gap on the order of a micrometer to increase the sensor capacitance value, thus improving the device resolution. Figure 12.15 shows a close-up view of the finger structure for a typical lateral accelerometer. Each movable finger forms differen-

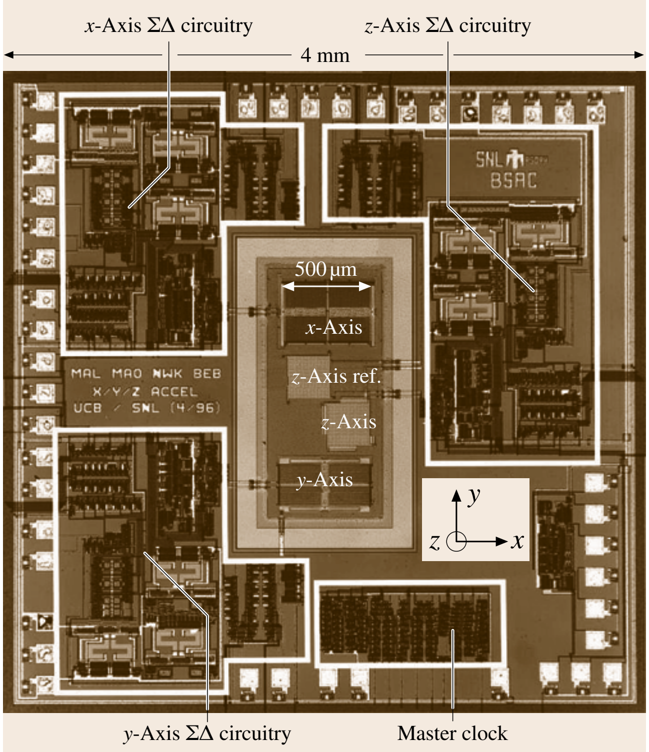

Fig. 12.16 Photo of a monolithic three-axis polysilicon surface-micromachined accelerometer with integrated interface and control electronics (after [12.18]) ◀

tial capacitances with two adjacent fixed fingers. This sensing capacitance configuration is attractive for interfacing with differential electronic detection circuits to suppress common-mode noise and other undesirable signal coupling. Monolithic accelerometers with a three-axis sensing capability integrated with on-chip electronic detection circuits have been realized using surfacing micromachining and CMOS microelectronics fabrication technologies [12.18]. Figure 12.16 shows a photo of one of these microsystem chips, which has an area of $4 \times 4\,\mathrm{mm}^2$. One vertical accelerometer and two lateral accelerometers are placed at the chip center with corresponding detection electronics along the periphery. A z-axis reference device, which is not movable, is used with the vertical sensor for electronic interfacing. The prototype system achieves a sensing resolution on the order of 1 mG with a 100 Hz bandwidth along each axis. The level of performance is adequate for automobile safety activation systems, vehicle stability and active suspension control, and various consumer products. Recently, monolithic MEMS accelerometers fabricated by using post-CMOS surface micromachining fabrication technology have been developed to achieve an acceleration noise floor of $50\,\mu\mathrm{g}/\sqrt{\mathrm{Hz}}$ [12.19]. This technology can enable MEMS capacitive inertial sensors to be integrated with interface electronics in a commercial CMOS process, thus minimizing prototyping cost.

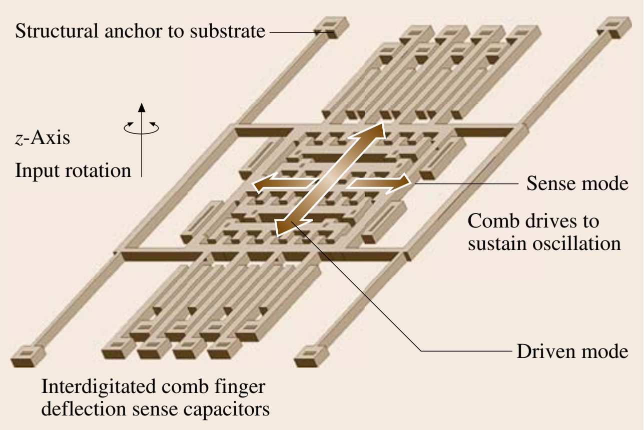

Fig. 12.17 Schematic of a vibratory rate gyroscope

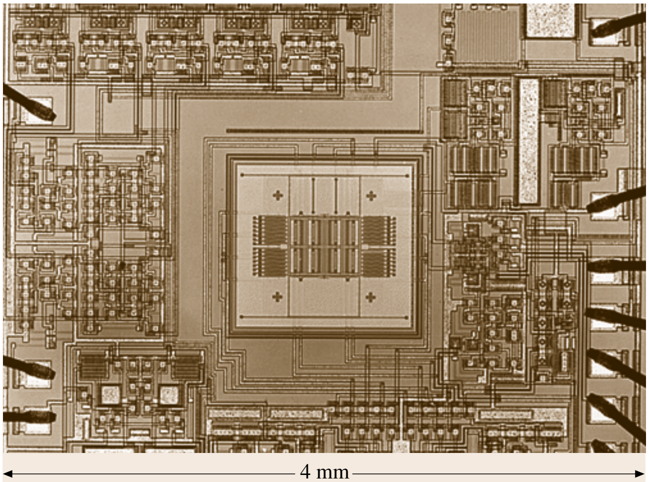

Fig. 12.18 Photo of a monolithic polysilicon surface-micromachined z-axis vibratory gyroscope with integrated interface and control electronics (after [12.20])

Gyroscope

Most of micromachined gyroscopes employ vibrating mechanical elements to sense rotations. The sensors rely on energy transfer between two vibration modes of a structure caused by Coriolis acceleration. Figure 12.17 presents a schematic of a z-axis vibratory rate gyroscope. The device consists of an oscillating mass electrostatically driven into resonance along the drive-mode axis using comb fingers. An angular rotation along the vertical axis (z-axis) introduces a Coriolis acceleration, which results in a structure deflection along the sense-mode axis, shown in the figure. The deflection changes the differential sense capacitance value, which can be detected as a measure of input angular rotation. A z-axis vibratory rate gyroscope operating upon this principle is fabricated using surface micromachining technology and integrated together with electronic detection circuits, as illustrated in Fig. 12.18 [12.20]. The micromachined sensor is fabricated using polysilicon structural material with a thickness around $2\,\mu\mathrm{m}$ and occupies an area of $1 \times 1\,\mathrm{mm}^2$. The sensor achieves a resolution of $\approx 1^\circ/(\mathrm{s}\sqrt{\mathrm{Hz}})$ under a vacuum pressure around 50 mTorr. Other MEMS single-axis gyroscopes integrated in commercial IC processes were demonstrated recently achieving an enhance performance [12.21, 22].

A dual-axis gyroscope based on a rotational disk at its resonance can be used to sense angular rotation along two lateral axes (x- and y-axis). Figure 12.19 shows a device schematic demonstrating the operating principle. A rotor disk supported by four mechanical suspensions can be driven into angular resonance along the z-axis. An input angular rotation along the x-axis will generate a Coriolis acceleration causing the disk to rotate along the y-axis, and vice versa. This

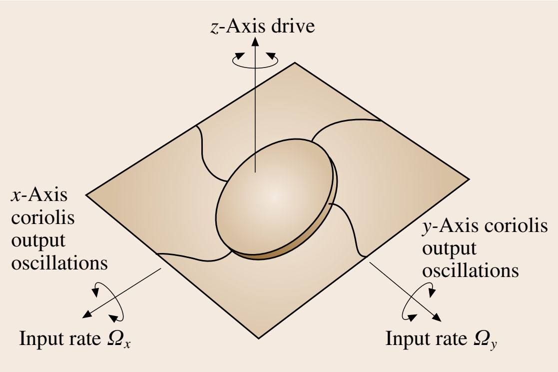

Fig. 12.19 Schematic of a dual-axis gyroscope

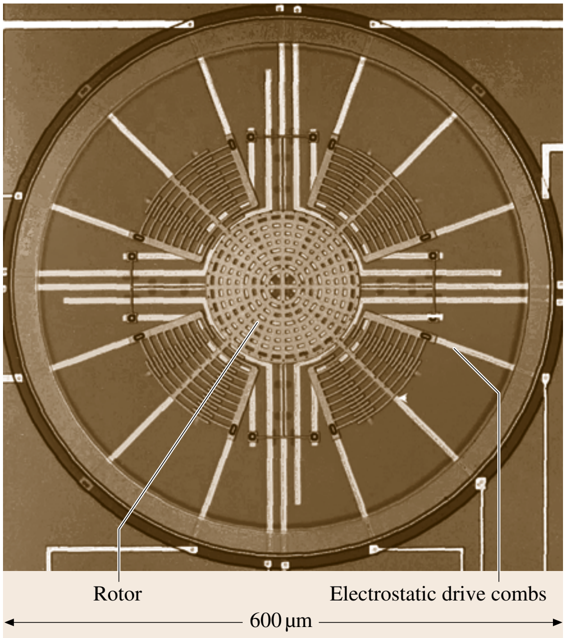

Fig. 12.20 Photo of a polysilicon surface-micromachined dual-axis gyroscope (after [12.23])

Coriolis-acceleration-induced rotation will change the sensor capacitance values between the disk and different sensing electrodes underneath. The capacitance change can be detected and processed by electronic interface circuits. Angular rotations along the two lateral axes can be measured simultaneously using this device architecture. Figure 12.20 shows a photo of a dual-axis gyroscope fabricated using a 2 µm thick polysilicon surface micromachining technology [12.23]. As shown in the figure, curved electrostatic drive combs are positioned along the circumference of the rotor dick to drive it into resonance along the vertical axis. The gyroscope exhibits a low random walk of $1°/\sqrt{\mathrm{h}}$ under a vacuum pressure around 60 mTorr. With accelerometers and gyroscopes each capable of three-axis sensing, a micormachine-based inertial measurement system providing a six-degree-of-freedom sensing capability can be realized. Figure 12.21 presents a photo of such a system containing a dual-axis gyroscope, a z-axis gyroscope, and a three-axis accelerometer chip integrated with microelectronic circuitry. Due to the precision in device layout and fabrication, the system can measure angular rotation and acceleration without the need to align individual sensors.

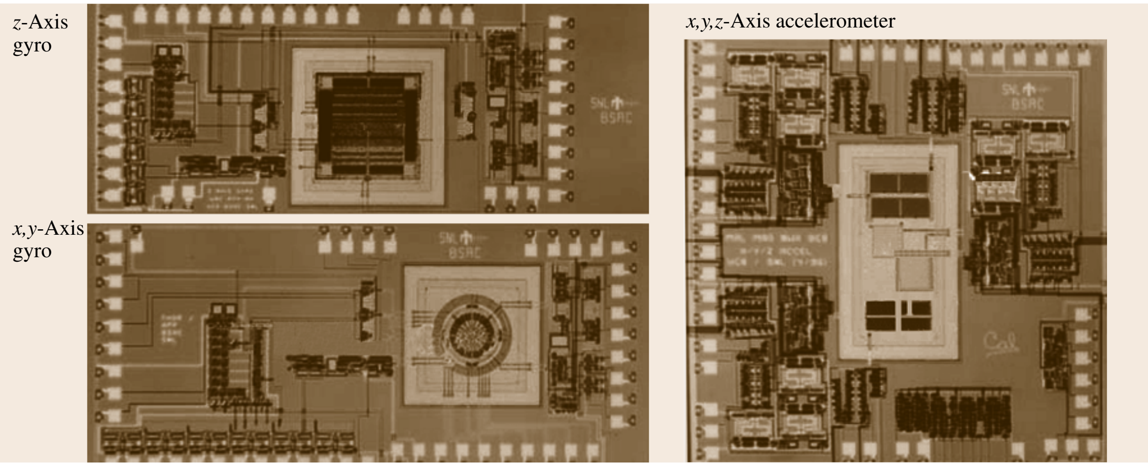

Fig. 12.21 Photo of a surface-micromachined inertial measurement system with a six-degree sensing capability

12.1.3 Optical MEMS

Surface micromachining has served as a key enabling technology to realize microeletromechancal optical devices for various applications ranging from sophisticated visual information displays and fiber-optic telecommunication to bar-code reading. Most of the existing optical systems are implemented using conventional optical components, which suffer from bulky size, high cost, large power consumption, poor efficiency and reliability issues. MEMS technology is promising for producing miniaturized, reliable, inexpensive optical components to revolutionize conventional optical systems [12.25]. In this section of the chapter, a few selected MEMS optical devices will be presented to illustrate their impact in the fields of visual display, precision optical platform, and data switching for optical communication.

Visual Display

An early MEMS device successfully used for various display applications is the Texas Instruments Digital Micromirror Device (DMD). The DMD technology can achieve higher performance in terms of resolution, brightness, contrast ratio, and convergence than the conventional cathode ray tube and is critical for digital high-definition television applications. A DMD consists of a large array of small mirrors with a typical area of $16 \times 16\,\mu m^2$ as illustrated in Fig. 12.22. A probe tip is shown in the figure for a size comparison. Figure 12.23 shows an SEM micrograph of a close-up view of a DMD pixel array [12.24]. Each mirror is capable of rotating by ±10° corresponding to either the *on* or *off* position due to an electrostatic actuation force. Light reflected from any on-mirrors passes through a projection lens and creates images on a large screen. Light from the remaining off-mirrors is reflected away from the projection lens to an absorber. The proportion of time during each video frame that a mirror remains in the on-state determines shades of gray, from black for zero on-time to white for a hundred percent on-time. Color can be added by a color wheel or a three-DMD chip setup. The three DMD chips are used for projecting red, green and blue colors. Each DMD pixel consists of a mirror connected by a mirror support post to an underlying yoke. The yoke in turn is connected by torsion hinges to hinge support posts, as shown in Fig. 12.24 [12.26]. The support post and hinges are hidden under the mirror to avoid light diffraction and thus improve contrast ratio and optical efficiency. There are two gaps on the order of a micrometer, one between the mirror and the underlying hinges and address electrodes, and a second between the coplanar address electrodes and hinges and an underlying metal layer from the CMOS static random access memory (SRAM) structure. The yoke is tilted over the second gap by an electrostatic actuation force, thus rotating the mirror plate. The SRAM determines which angle the mirror needs to be tilted by applying proper actuation voltages to the mirror and address electrodes. The DMD is fabricated using an aluminum-based surface micromachining technology. Three layers of aluminum thin film are deposited and patterned to form the mirror and its suspension system. Polymer material is used as sacrifi-

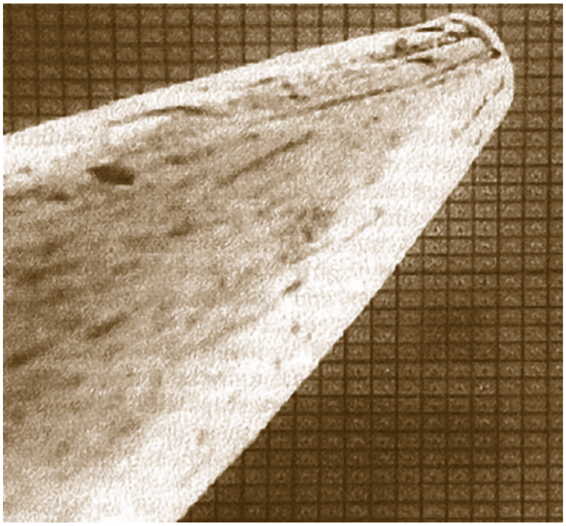

Fig. 12.22 Photo of a digital micromirror device (DMD) array (© Texas Instruments)

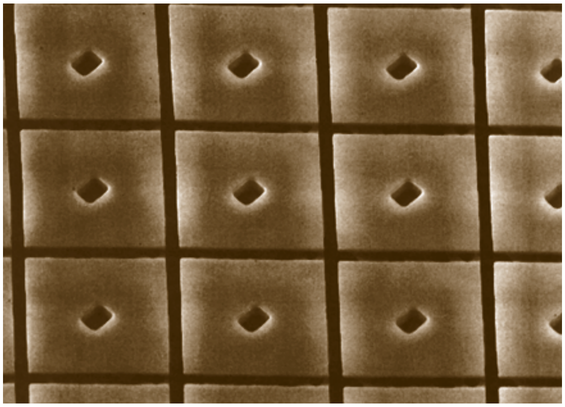

Fig. 12.23 SEM micrograph of a close-up view of a DMD pixel array (after [12.24])

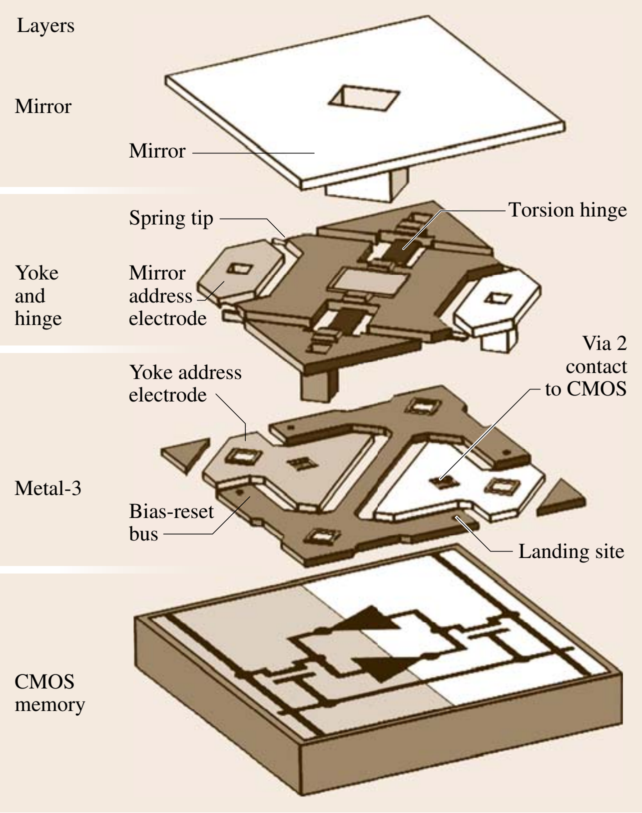

Fig. 12.24 Detailed structure layout of a DMD pixel (after [12.26])

cial layer and is removed by a plasma etch at the end of the process to freely release the micromirror structure. The micromachining process is compatible with standard CMOS fabrication, allowing the DMD to be monolithically integrated with a mature CMOS address circuit technology, thus achieving high yield and low cost. Figure 12.25 shows an SEM micrograph of a fabricated DMD pixel revealing its cross section after an ion milling. A close-up view on the yoke and hinge support under the mirror is shown in Fig. 12.26.

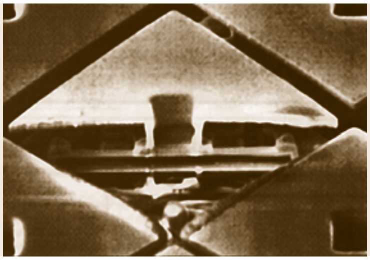

Fig. 12.25 SEM micrograph of a DMD pixel after removing half of the mirror plate using ion milling (© Texas Instruments)

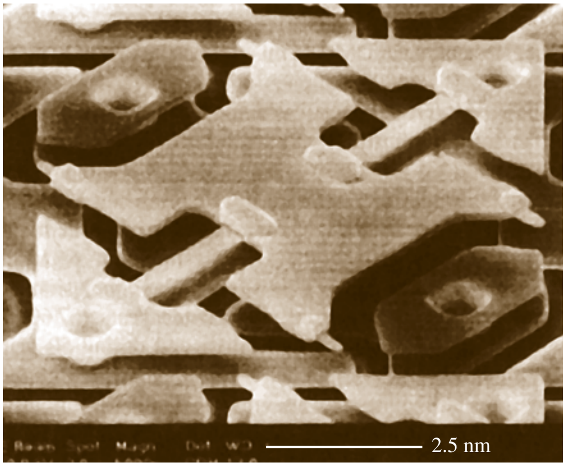

Fig. 12.26 SEM micrograph of a close-up of a DMD yoke and hinges (after [12.26])

Precision Optical Platform

The growing optical communication and measurement industry require low-cost, high-performance optoelectronic modules such as laser-to-fiber couplers, scanners, interferometers, etc. A precision alignment and the ability to actuate optical components such as mirrors, gratings, and lenses with sufficient accuracy are critical for high-performance optical applications. Conventional hybrid optical integration approaches, such as the silicon-optical-bench, suffers from a limited alignment tolerance of ±1 μm and also lacks of component actuation capability [12.27, 28]. As a result, only simple optical systems can be constructed with no more than a few components, thus severely limiting the performance. Micromachining, however, provides a critical enabling technology, allowing movable optical components to be fabricated on a silicon substrate. Component movement with high precision can be achieved through electrostatic actuation. By combining micromachined movable optical components with lasers, lenses, and fibers on the same substrate, an on-chip complex self-aligning optical system can be realized. Figure 12.27a shows an SEM micrograph of a surface-micromachined, electrostatically actuated microreflector for laser-to-fiber coupling and external-cavity-laser applications [12.29]. The device consists of a polysilicon mirror plate hinged to a support beam. The mirror and the support, in turn, are hinged to a vibromotor-actuator slider. The microhinge technol-

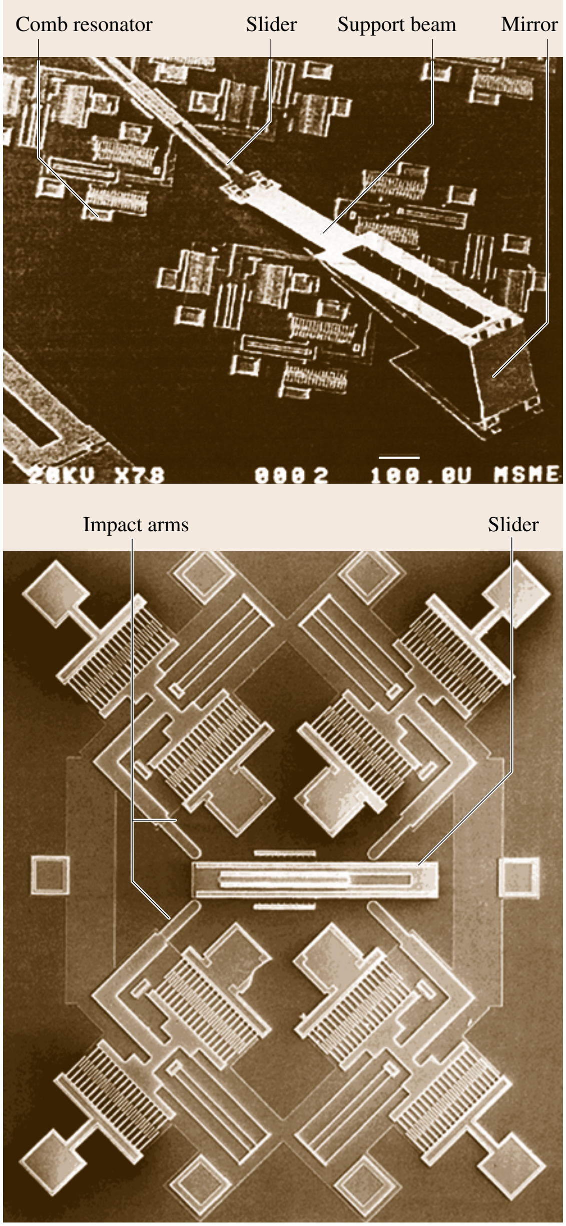

Fig. 12.27 (a) SEM micrograph of a surface-micromachined, electrostatically actuated microreflector; **(b)** SEM micrograph of a surface-micromachined vibromotor (after [12.29])

ogy [12.30] allows the joints to rotate out of the substrate plane to achieve large aspect ratios. Common-mode actuation of the sliders results in a translational motion, while differential slider motion produces an out-of-plane mirror rotation. These motions permit the microreflector to redirect an optical beam in a desirable location. Each of the two slides is actuated with an integrated microvibromotor shown in Fig. 12.27b. The vibromotor consists of four electrostatic comb resonators with attached impact arms driving a slider through oblique impact. The two opposing impacters are used for each travel direction to balance the forces. The resonator is a capacitively driven mass anchored to the substrate through a folded beam flexure. The flexure compliance determines the resonant frequency and travel range of the resonator. When the comb structures are driven at their resonant frequency (around 8 kHz), the slider exhibits a maximum velocity of over 1 mm/s. Characterization of the vibromotor also shows that a slider step resolution of less than 0.3 μm can be achieved [12.31], making it attractive for precision alignment of various optical components. The prototype microreflector can obtain an angular travel range over 90° and a translational travel range of 60 μm. By using this device, beam steering, fiber coupling, and optical scanning have been demonstrated.

Optical Data Switching

High-speed communication infrastructures are highly desirable for transferring and processing real-time voice and video information. Optical fiber communication technology has been identified as the critical backbone to support such systems. A high-performance optical data switching network, which routes various optical signals from sources to destinations, is one of the key building blocks for system implementation. At present, optical signal switching is performed by using hybrid optical-electronic-optical (O-E-O) switches. These devices first convert incoming light from input fibers to electrical signals first and then route the electrical signals to the proper output ports after signal analyses. At the output ports, the electrical signals are converted back to streams of photons or optical signals for further transmission over the fibers. The O-E-O switches are expensive to build, integrate, and maintain. Furthermore, they consume substantial amount of power and introduce additional latency. It is therefore highly desirable to develop an all-optical switching network in which optical signals can be routed without intermediate conversion into electrical form, thus minimizing power dissipation and system delay. While a number of approaches are being considered for building all-optical switches, MEMS technology is attractive because it can provide arrays of tiny movable mirrors which can redirect incoming beams from input fibers

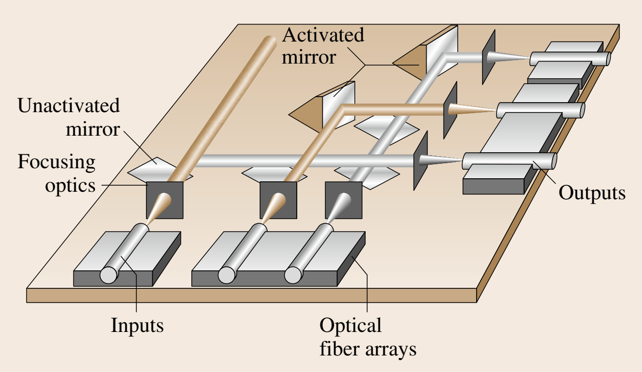

Fig. 12.28 Schematic of a two-dimensional micromirror-based fiber optic switching matrix

to corresponding output fibers. As described in the previous sections, these micromirrors can be batch fabricated using silicon micromachining technologies, thus achieving an integrated solution with the potential for low cost. A significant reduction in power dissipation is also expected.

Figure 12.28 shows an architecture of a two-dimensional micromirror array forming a switching matrix with rows of input fibers and columns of output fibers (or vice versa). An optical beam from an input fiber can be directed to an output fiber through activating the corresponding reflecting micromirror. Switches with eight inputs and eight outputs can be readily implemented using this technique, which can be further extended to a 64×64 matrix. The micromirrors are moved between two fixed stops by digital control, thus eliminating the need for precision motion control. Figure 12.29 presents an SEM micrograph of a simple 2×2 MEMS fiber optic switching network prototype for an illustration purpose [12.32]. The network includes a mirror chip passively integrated with a silicon submount, which contains optical fibers and ball lenses. The mirror chip consists of four surface-micromachined vertical torsion mirrors. The four mirrors are arranged such that in the *reflection* mode, the input beams are reflected by two 45° vertical torsion mirrors and coupled into the output fibers located on the same side of the chip. In the *transmission* mode, the vertical torsion mirrors are rotated out of the optical paths, thus allowing the input beams to be coupled into the opposing output fibers. Figure 12.30 shows an SEM micrograph of a polysilicon vertical torsion mirror. The device consists of a mirror plate attached to a vertical supporting frame by torsion beams and a vertical back electrode plate. The mirror plate is ≈ 200 µm wide, 160 µm long, and 1.5 µm thick. The mirror surface is coated with a thin layer of gold to improve the optical reflectivity. The back plate is used to electrostatically actuate the mirror plate so that the mirror can be rotated out of the optical path in the *transmission* mode. Surface micromachining with microhinge technology is used to realize the overall structure. The back electrode plate is integrated with a scratch drive actuator array [12.33] for self-assembly. The self-assembly approach is critical when multiple vertical torsion mirrors are used to implement more advanced functions.

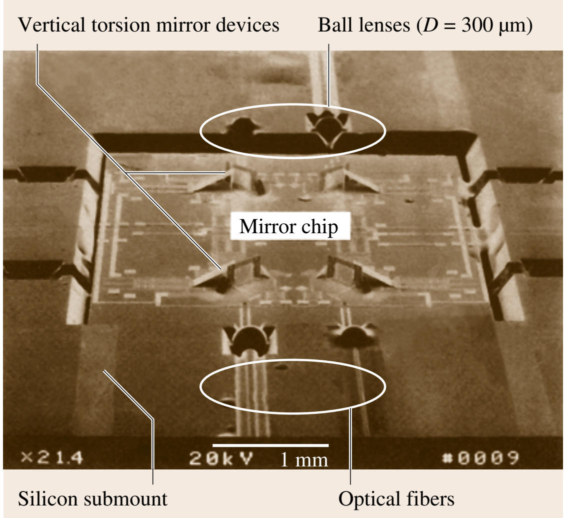

Fig. 12.29 SEM micrograph of a 2×2 MEMS fiber optic switching network (after [12.32])

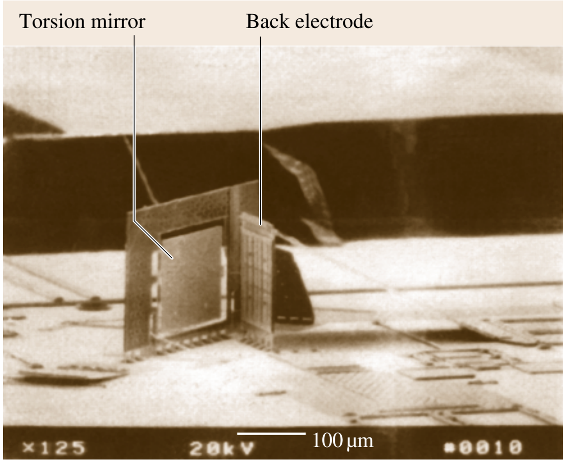

Fig. 12.30 SEM micrograph of a polysilicon surface-micromachined vertical torsion mirror (after [12.32])

A more sophisticated optical switching network with a large scaling potential can be implemented by using a three-dimensional (3-D) switching architecture as shown in Fig. 12.31. The network consists of arrays of two-axis mirrors to steer optical beams from input fibers to output fibers. A precision analog closed-loop mirror position control is required to accurately direct a beam along two angles so that one input fiber can be optically connected to any output fiber. The optical length depends little on which set of fibers are connected, thus achieving a more uniform switching characteristic, which is critical for implementing large scale network. Two-axis mirrors are the crucial components for implementing the 3-D architecture. Figure 12.32 shows an SEM micrograph of a surface-micromachined two-axis beam-steering mirror positioned by using self-assembly technique [12.34]. The self-assembly is accomplished during the final release step of the mirror processing sequence. Mechanical energy is stored in a special high-stress layer during the deposition, which is put on top of the four assembly arms. Immediately after the assembly arms are released, the tensile stress in this layer causes the arms to bend up, pushing the mirror frame and lifting it above the silicon substrate. All mirrors used in the switching network can be fabricated simultaneously without any human intervention or external power supply.

12.1.4 RF MEMS

The increasing demand for wireless communication applications, such as cellular and cordless telephony, wireless data networks, two-way paging, global positioning system, etc., motivates a growing interest in building miniaturized wireless transceivers with multistandard capabilities. Such transceivers will greatly enhance the convenience and accessibility of various wireless services independent of geographic location. Miniaturizing current single-standard transceivers, through a high-level of integration, is a critical step towards building transceivers that are compatible with multiple standards. Highly integrated transceivers will also result in reduced package complexity, power consumption, and cost. At present, most radio transceivers rely on a large number of discrete frequency-selection components, such as radio-frequency (RF) and intermediate-frequency (IF) band-pass filters, RF voltage-controlled oscillators (VCOs), quartz crystal oscillators, solid-state switches, etc. to perform the necessary analog signal processing. Figure 12.33 shows a schematic of

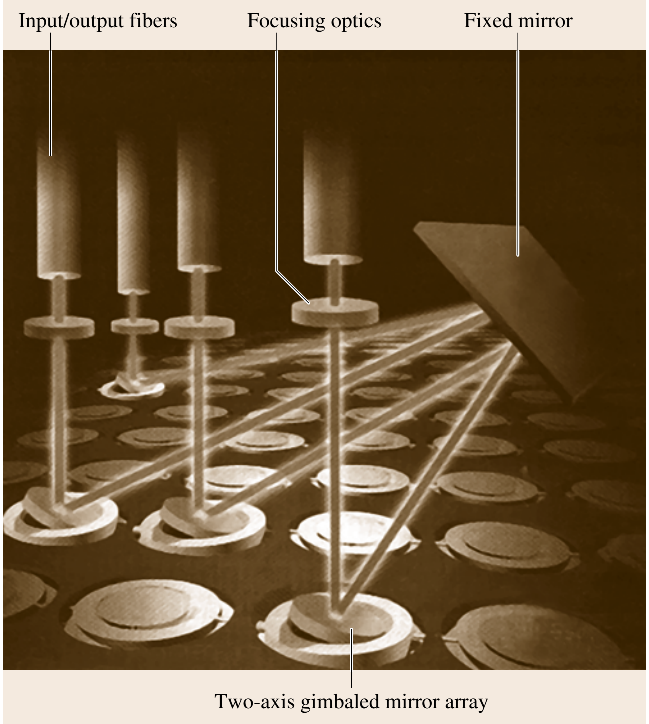

Fig. 12.31 Schematic of a three-dimensional micromirror-based fiber optic switching matrix

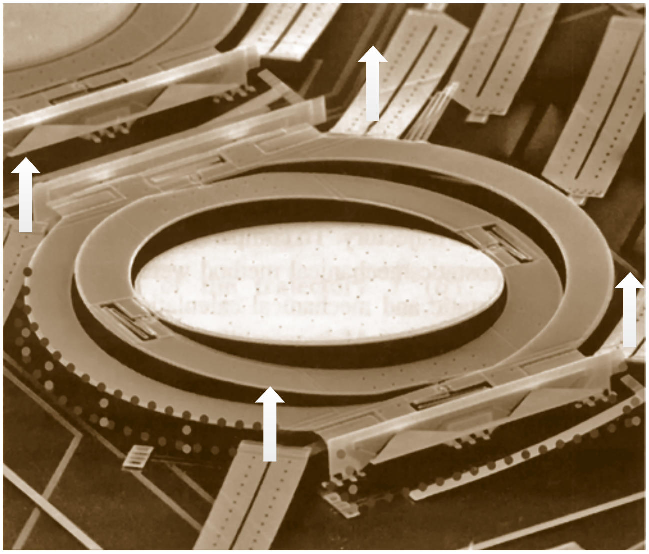

Fig. 12.32 SEM micrograph of a surface-micromachined two-axis beam-steering micromirror positioned using a self-assembly technique (after [12.34])

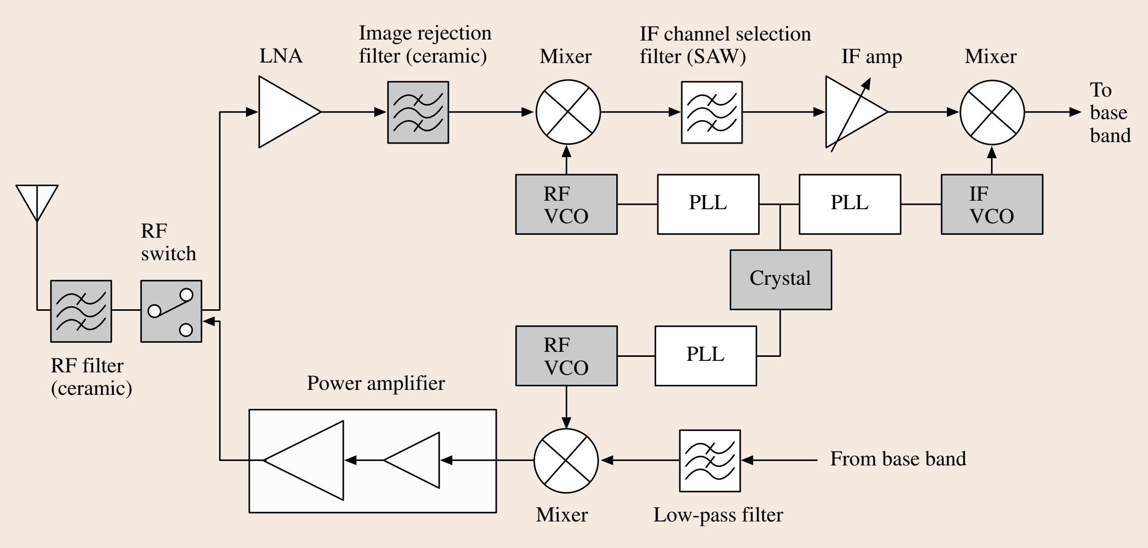

Fig. 12.33 Schematic of a superheterodyne radio architecture

a superheterodyne radio architecture, in which discrete components are shaded in dark color. Theses off-chip devices occupy the majority of the system area, thus severely hindering transceiver miniaturization. MEMS technology, however, offers a potential solution to integrate these discrete components onto silicon substrates with microelectronics, achieving a size reduction of a few orders of magnitude. It is therefore expected to become an enabling technology to ultimately miniaturize radio transceivers for future wireless communications.

MEMS Variable Capacitors

Integrated high-performance variable capacitors are critical for low noise VCOs, antenna tuning, tunable matching networks, etc. Capacitors with high quality factors (Q), large tuning range and linear characteristics are crucial for achieving system performance requirements. On-chip silicon PN junction and MOS based variable capacitors suffer from low quality factors (below 10 at 1 GHz), limited tuning range and poor linearity, thus are inadequate for building high-performance transceivers. MEMS technology has demonstrated monolithic variable capacitors achieving stringent performance requirements. These devices typically reply on an electrostatic actuation method to vary the air gap between a set of parallel plates [12.35–38] or vary the capacitance area between a set of conductors [12.39] or mechanically displace a dielectric layer

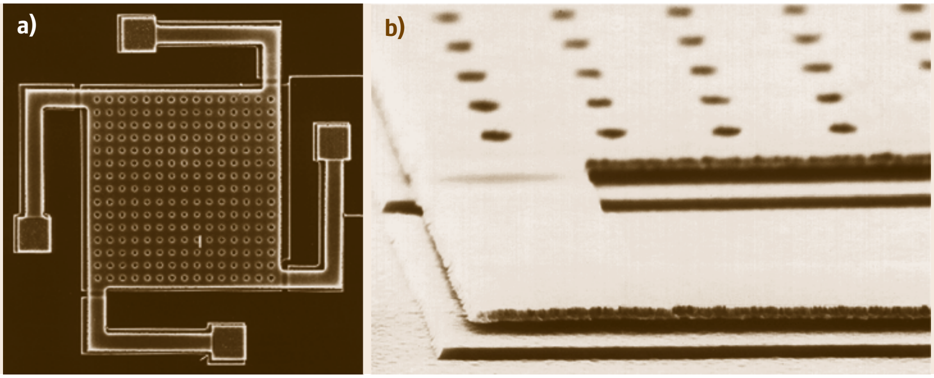

Fig. 12.34 **(a)** SEM micrograph of a top view of an aluminum surface-micromachined variable capacitor; **(b)** SEM micrograph of a cross-sectional view of the variable capacitor (after [12.35])

in an air-gap capacitor [12.40]. Improved tuning ranges have been achieved with various device configurations. Figure 12.34 shows SEM micrographs of an aluminum micromachined variable capacitor fabricated on a silicon substrate [12.35]. The device consists of a 200 × 200 μm^2 aluminum plate with a thickness of 1 μm suspended above the bottom electrode by an air gap of 1.5 μm. Aluminum is selected as the structural material due to its low resistivity, critical for achieving a high quality factor at high frequencies. A DC voltage applied across the top and bottom electrodes introduces an electrostatic pull-down force, which pulls the top plate towards the bottom electrode, thus changing the device capacitance value. The capacitors are fabricated using aluminum-based surface micromachining technology. Sputtered aluminum is used for building the capacitor top and bottom electrodes. Photoresist is served as the sacrificial layer, which is then removed through an oxygen-based plasma dry etch to release the microstructure. The processing technology requires a low thermal budget, thus allowing the variable capacitors to be fabricated on top of wafers with completed electronic circuits without degrading the performance of active devices. Figure 12.35 presents an SEM micrograph of four MEMS tunable capacitors connected in parallel. This device achieves a nominal capacitance value of 2 pF and a tuning range of 15% with 3 V. A quality factor of 62 has been demonstrated at 1 GHz, which matches or exceeds that of discrete varactor diodes and is at least an order of magnitude larger than that of a typical junction capacitor implemented in a standard IC process.

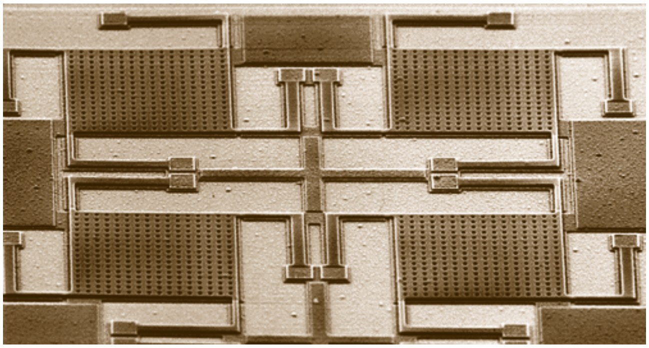

Fig. 12.35 SEM micrograph of four MEMS aluminum variable capacitors connected in parallel (after [12.35])

MEMS tunable capacitors based upon varying capacitance area between a set of conductors have been demonstrated. Figure 12.36 shows an SEM micrograph of a such device [12.39]. The capacitor comprises arrays of interdigitated electrodes, which can be electrostatically actuated to vary the electrode overlap area. A close-up view of the electrodes is shown in Fig. 12.37. The capacitor is fabricated using a silicon-

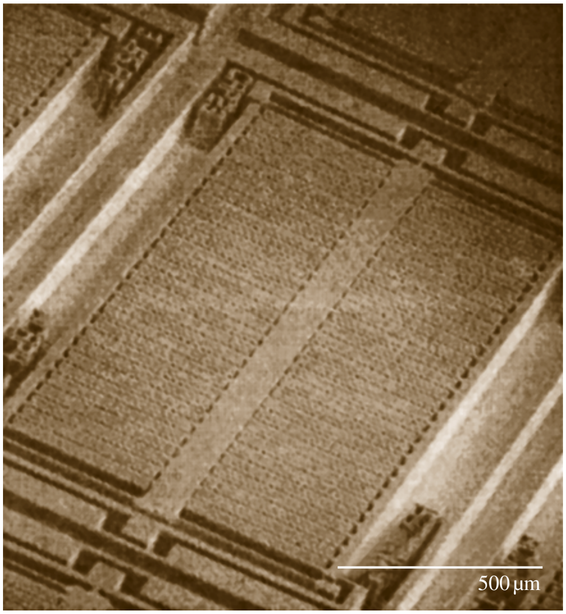

Fig. 12.36 SEM micrograph of a silicon tunable capacitor using a comb drive actuator (after [12.39])

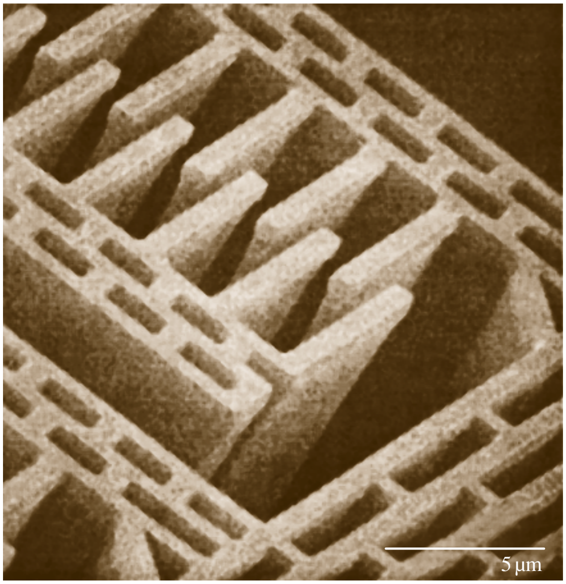

Fig. 12.37 SEM micrograph of a close view of a tunable capacitor comb fingers (after [12.39])

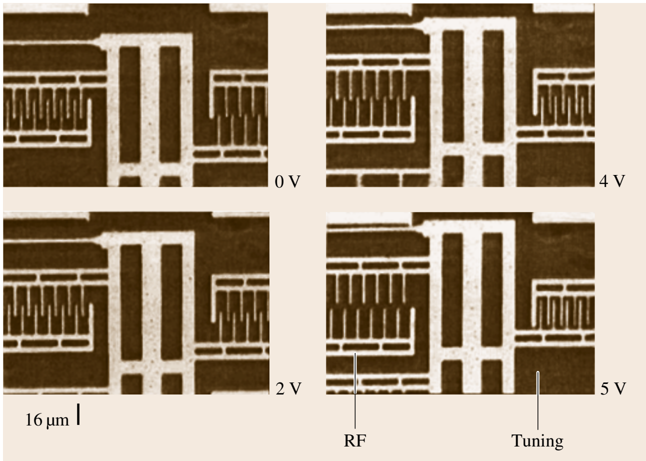

Fig. 12.38 Photos of comb fingers at different actuation voltages (after [12.39])

on-insulator (SOI) substrate with a top silicon layer thickness around 20 µm to obtain a high aspect ratio for the electrodes, critical for achieving a large capacitance density and reduced tuning voltage. The silicon layer is etched to form the device structure followed by removing the underneath oxide to release the capacitor. A thin aluminum layer is then sputtered over the capacitor to reduce the series resistive loss. The device exhibits a quality factor of 34 at 500 MHz and can be tuned between 2.48 and 5.19 pF with an actuation voltage under 5 V, corresponding to a tuning range over 100%. Figure 12.38 shows the variation of electrode overlap area under different tuning voltages.

Tunable capacitors relying on a movable dielectric layer have been fabricated using MEMS technology. Figure 12.39 presents an SEM micrograph of a copper-based micromachined tunable capacitor [12.40]. The device consists of an array of copper top electrodes suspended above a bottom copper plate with an air gap of ≈ 1 µm. A thin nitride layer is deposited, patterned, and suspended between the two copper layers by lateral mechanical spring suspensions after sacrificial release. A DC voltage applied across the copper layers introduces a lateral electrostatic pull-in force on the nitride, thus resulting in a movement which changes the overlapping area between each copper electrode and the bottom plate, and hence the device capacitance. The tunable capacitor achieves a quality factor over 200 at 1 GHz with 1 pF capacitance due to the highly conductive copper layers and a tuning range around 8% with 10 V.

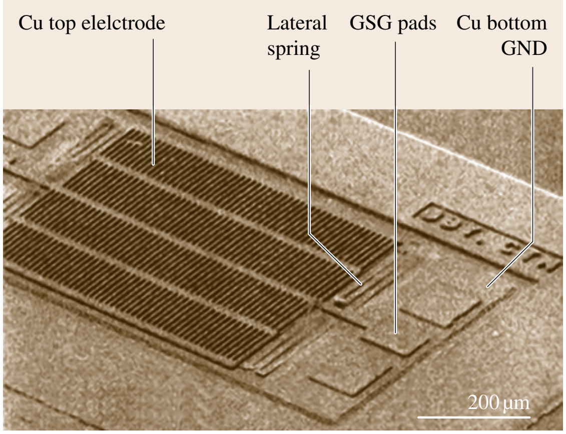

Fig. 12.39 SEM micrograph of a copper surface-micromachined tunable capacitor with a movable dielectric layer (after [12.40])

Micromachined Inductors

Integrated inductors with high quality factors are as critical as the tunable capacitors for high performance RF system implementation. They are the key components for building low-noise oscillators, low-loss matching networks, etc. Conventional on-chip spiral inductors suffer from limited quality factors of around 5 at 1 GHz, an order of magnitude lower than the required val-

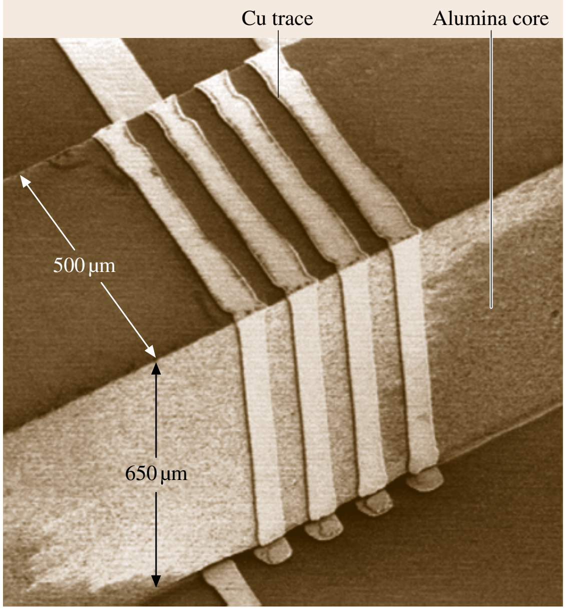

Fig. 12.40 SEM micrograph of a 3-D coil inductor fabricated on a silicon substrate (after [12.41])

ues from discrete counterparts. The poor performance is mainly caused by substrate loss and metal resistive loss at high frequencies. Micromachining technology provides an attractive solution to minimize these loss contributions; hence enhancing the device quality factors. Figure 12.40 shows an SEM micrograph of a 3-D coil inductor fabricated on a silicon substrate [12.41]. The device consists of 4-turn 5 µm thick copper traces electroplated around an insulting core with a 650 µm by 500 µm cross section. Compared to spiral inductors, this geometry minimizes the coil area which is in close proximity to the substrate and hence the eddy-current loss, resulting in a maximized Q-factor and device self-resonant frequency. Copper is selected as the interconnect metal because of its low sheet resistance, critical for achieving a high Q-factor. The inductor achieves a 14 nH inductance value with a quality factor of 16 at 1 GHz. A single-turn 3-D device exhibits a Q-factor of 30 at 1 GHz, which matches the performance of discrete counterparts. The high-Q 3-D inductor and MEMS tunable capacitors, shown in Fig. 12.35, have been employed to implement a RF CMOS VCO achieving a low phase noise performance suitable for typical wireless communication applications such as GMS cellular telephony [12.42].

Other 3-D inductor structures such as the levitated spiral inductors have been demonstrated using micromachining fabrication technology. Figure 12.41 shows an SEM micrograph of a levitated copper inductor, which is suspended above the substrate through supporting posts [12.44]. The levitated geometry can minimize the substrate loss, thus achieving an improved quality factor. The inductor shown in the figure achieves a 1.4 nH inductance value with a Q-factor of 38 at 1.8 GHz using a glass substrate. Similar inductor structures have been demonstrated on standard silicon substrates achieving a nominal inductance value of ≈ 1.4 nH with a Q-factor of 70 measured at 6 GHz [12.45].

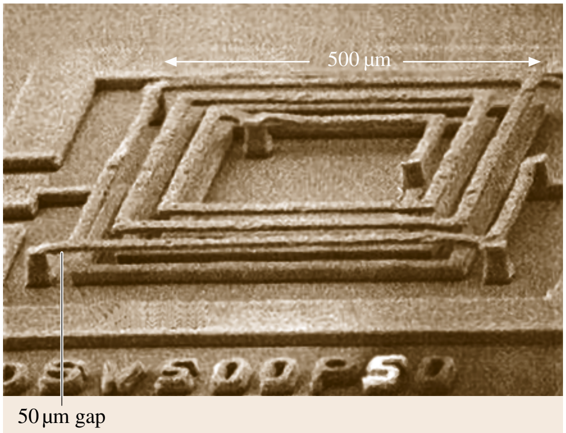

Fig. 12.41 SEM micrograph of a levitated spiral inductor fabricated on a glass substrate (after [12.40])

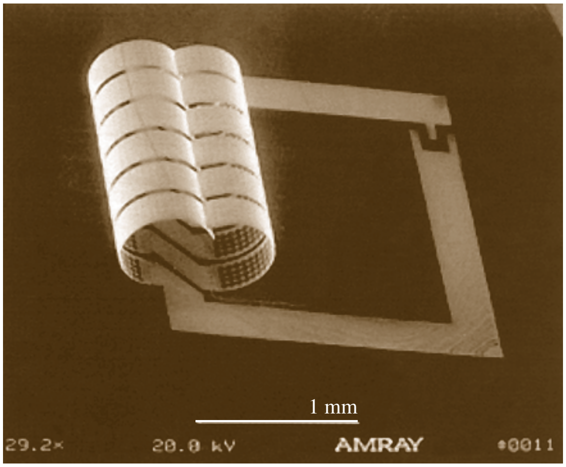

Fig. 12.42 SEM micrograph of a self-assembled out-of-plane coil inductor (after [12.43])

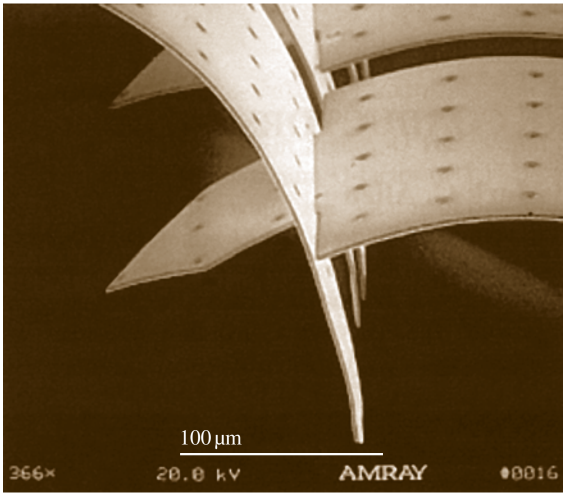

Fig. 12.43 SEM micrograph of an interlocking trace from a self-assembled out-of-plane oil inductor (after [12.43])

A self-assembled out-of-plane coil has been fabricated using micromachining technology. The inductor winding traces are made of refractory metals with controlled built-in stress such that the traces can curl out of the substrate surface upon release and interlock into each other to form coil windings. Figure 12.42 shows an SEM micrograph of a self-assembled out-of-plane coil inductor [12.43]. A close-up view of an interlocking trace is shown in Fig. 12.43. Copper is plated on the interlocked traces to form highly conductive windings at the end of processing sequence. The inductor shown in Fig. 12.42 achieves a quality factor around 40 at 1 GHz.

MEMS Switches

The microelectromechanical switch is another potentially attractive miniaturized component enabled by micromachining technologies. These switches offer superior electrical performance in terms of insertion loss, isolation, linearity, etc., and are intended to replace off-chip solid-state counterparts, which provide switching between the receiver and transmitter signal paths. They are also critical for building phase shifters, tunable antennas, and filters. The MEMS switches can be characterized into two categories: capacitive and metal-to-metal contact types. Figure 12.44 presents a cross-sectional schematic of an RF MEMS capacitive switch. The device consists of a conductive membrane, typically made of aluminum or gold alloy suspended above a coplanar electrode by an air gap of a few micrometers. For RF or microwave applications, actual metal-to-metal contact is not necessary; rather, a step change in the plate-to-plate capacitance realizes the switching function. A thin silicon nitride layer with a thickness on the order of 1000 Å is typically deposited above the bottom electrode. When the switch is in the on-state, the membrane is high resulting in a small plate-to-plate capacitance; hence, a minimum high-frequency signal coupling (high isolation) between the two electrodes. In the off-state (with a large enough applied DC voltage), the switch provides a large capacitance due to the thin dielectric layer, thus causing a strong signal coupling (low insertion loss). The capacitive switch consumes near-zero power, which is attractive for low power portable applications. Switching cycles over millions for this type of device have been demonstrated. Figure 12.45 shows a top view photo of a fabricated MEMS capacitive switch [12.46]. Surface micromachining technology, using metal for the electrodes and polymer as the sacrificial layer, is used to fabricate the device. The switch can be actuated with a DC voltage on the order of 50 V and exhibits a low insertion loss of ≈ -0.28 dB at 35 GHz and a high isolation of −35 dB at the same frequency.

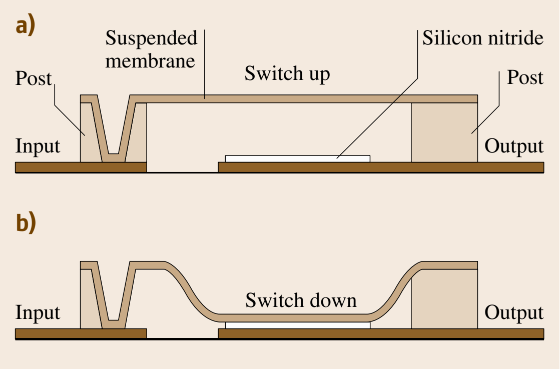

Fig. 12.44 Cross-sectional schematics of an RF MEMS capacitive switch

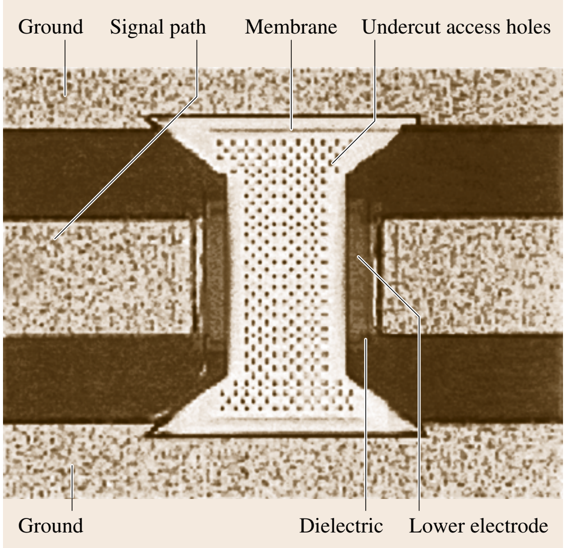

Fig. 12.45 Top view photo of a fabricated RF MEMS capacitive switch (after [12.46])

Metal-to-metal contact switches are important for interfacing large bandwidth signals including DC. This type of device typically consists of a cantilever beam or clamped-clamped bridge with a metallic contact pad positioned at the beam tip or underneath bridge center. Through an electrostatic actuation, a contact can be formed between the suspended contact pad and an underlying electrode on the substrate [12.47–49]. Figure 12.46 shows a cross-sectional schematic of a metal-to-metal contact switch [12.49]. The top view of the fabricated device is presented in Fig. 12.47. The switch exhibits an actuation voltage of 30 V, a response time of 20 μs, and mechanical strength to withstand 10^9 actuations. An isolation greater than 50 dB below 2 GHz and insertion loss less than 0.2 dB from DC through 40 GHz has been demonstrated. Metal-to-metal contact switches relying on electrothermal actuation method have also

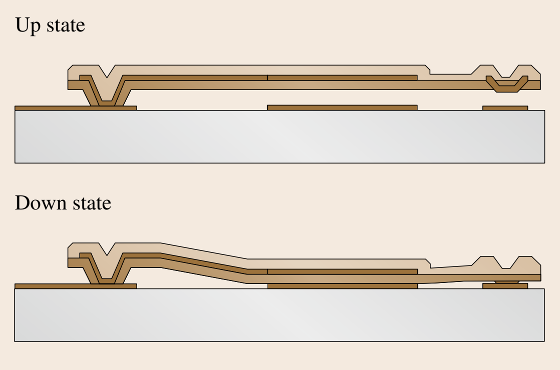

Fig. 12.46 Cross-sectional schematic of a metal-to-metal contact switch (after [12.49])

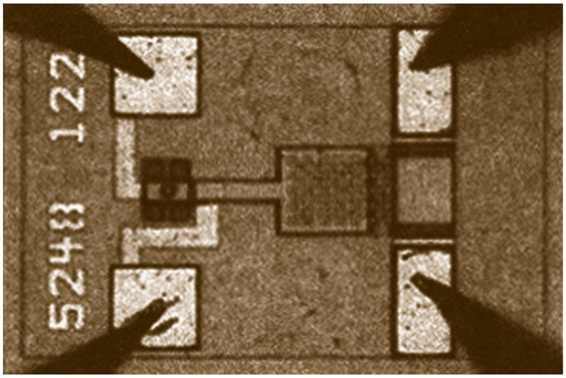

Fig. 12.47 Top view photo of a fabricated metal-to-metal contact switch (after [12.49])

been developed to demonstrate a low actuation voltage around 3 V, however, at an expense of reduced switching speed of 300 µs and increased power dissipation in the range of 60–100 mW [12.50, 51]. The fabricated switches achieve an off-state isolation of −20 dB at 40 GHz and an insertion loss of −0.1 dB up to 50 GHz.

MEMS Resonators

Microelectromechanical resonators based upon polysilicon comb-drive structures, suspended beams, and center-pivoted disk configurations have been demonstrated for performing analog signal processing [12.50, 52–56]. These microresonators can be excited into mechanical resonance through an electrostatic drive. The mechanical motion causes a change of device capacitance resulting in an output electrical current when a proper DC bias voltage is used. The output current exhibits the same frequency as the mechanical resonance, thus achieving an electrical filtering function through the electromechanical coupling. Micromachined polysilicon flexural-mode mechanical resonators have demonstrated a quality factor greater than 80 000 in a 50 µTorr vacuum [12.57]. This level of performance is comparable to a typical quartz crystal and is thus attractive for implementing monolithic low-noise and low-drift reference signal sources. Figure 12.48 shows an SEM micrograph of a surface-micromachined comb drive resonator integrated with CMOS sustaining electronics on a same substrate to form a monolithic high-Q MEMS resonator-based oscillator [12.52]. The oscillator achieves an operating frequency of 16.5 KHz with a clean spectral purity. A chip area of $\approx 420 \times 230\,\mu\text{m}^2$ is consumed for fabricating the overall system, representing a size reduction by orders of magnitude compared to conventional quartz crystal oscillators.

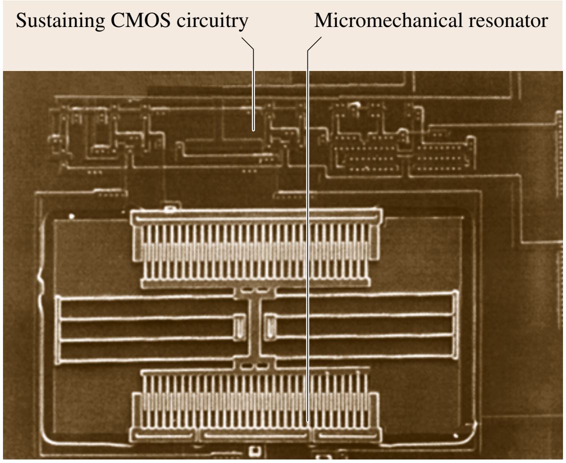

Fig. 12.48 SEM micrograph of a surface-micromachined comb drive resonator integrated with CMOS sustaining electronics (after [12.52])

Micromachined high-Q resonators can be coupled to implement low-loss frequency selection filters. Figure 12.49 shows an SEM micrograph of a surface-micromachined polysilicon two-resonator, spring-coupled bandpass micromechanical filter [12.54]. The filter consists of two silicon micromechanical clamped-clamped beam resonators, coupled mechanically by a soft spring, all suspended 0.1 µm above the substrate. Polysilicon strip lines underlie the central regions of each resonator and serve as capacitive transducer electrodes positioned to induce resonator vibration in a direction perpendicular to the substrate. Under a normal operation, the device is excited capacitively by a signal voltage applied to the input electrode.

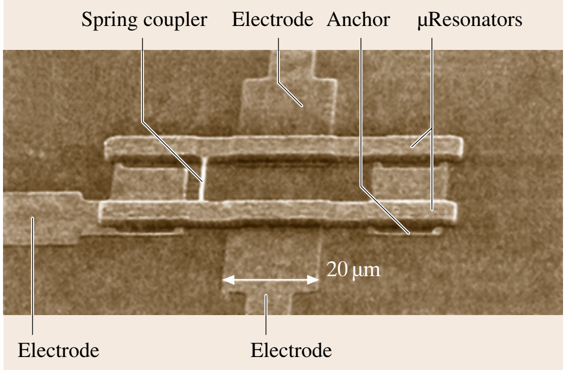

Fig. 12.49 SEM micrograph of a polysilicon surface-micromachined two-resonator spring-coupled bandpass micromechanical filter (after [12.54])

The output is taken at the other end of the structure, also by capacitive transduction. The filter achieves a center frequency of 7.81 MHz, a bandwidth of 0.23%, and an insertion loss less than 2 dB. The achieved performance is attractive for implementing filters in the low MHz range.

To obtain a higher mechanical resonant frequency with low losses, a surface-micromachined contour-mode disk resonator has been proposed, as shown in Fig. 12.50 [12.56]. The resonator consists of a polysilicon disk suspended 5000 Å above the substrate with a single anchor at its center. Plated metal input electrodes surround the perimeter of the disk with a narrow separation of around 1000 Å, which defines the capacitive, electromechanical transducer of the device. To operate the device, a DC bias voltage is applied to the structure with an AC input signal applied to the electrodes, resulting in a time varying electrostatic force acting radially on the disk. When the input signal matches the device resonant frequency, the resulting electrostatic force is amplified by the Q-factor of the resonator, producing expansion and contraction of the disk along its radius. This motion, in turn, produces a time-varying output current at the same frequency, thus achieving the desirable filtering. The prototype resonator demonstrates an operating frequency of 156 MHz with a Q-factor of 9400 in vacuum. The increased resonant frequency is comparable to the first intermediate frequency used in a typical wireless transceiver design and is thus suitable for implementing IF bandpass filters. Recently, self-aligned MEMS fabrication technique was developed to demonstrate vibrating radial-contour mode polysilicon micromechanical disk resonators with resonant frequencies up to 1.156 GHz and measured Q's close to 3000 in both vacuum and air [12.51]. The achieved performance is attractive for potentially replacing RF frequency selection filters in current wireless transceivers with MEMS versions.

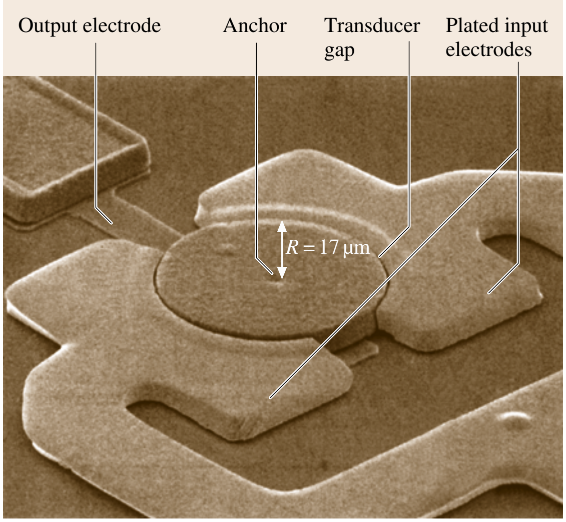

Fig. 12.50 SEM micrograph of a polysilicon surface-micromachined contour-mode disk resonator (after [12.56])

12.2 Nanoelectromechanical Systems (NEMS)

Unlike their microscale counterparts, nanoelectromechanical systems (NEMS) are made of electromechanical devices that have critical structural dimensions at or below 100 nm. These devices are attractive for applications where structures of very small mass and/or very large surface area-to-volume ratios provide essential functionality, such as force sensors, chemical sensors, biological sensors, and ultrahigh frequency resonators to name a few. NEMS fabrication processes can be classified into two general categories based on the approach used to create the structures. *Top-down* approaches utilize submicrometer lithographic techniques to fabricate device structures from *bulk* material, either thin films or thick substrates. *Bottom-up* approaches involve the fabrication of nanoscale devices in much the same way that nature constructs objects, by sequential assembly using atomic and/or molecular building blocks. While advancements in bottom-up approaches are developing at a very rapid pace, most advanced NEMS devices are currently created utilizing top-down techniques that combine existing process technologies, such as electron-beam lithography, conventional film growth and chemical etching. Top-down approaches make integration with microscale packaging relatively straightforward since the only significant difference between the nanoscale and microscale processing steps is the method used to pattern the various features.

In large measure, NEMS has followed a developmental path similar to the route taken in the development of MEMS in that both have leveraged existing processing techniques from the IC industry. For instance, the electron-beam lithographic techniques used in top-down NEMS fabrication are the same techniques that have become standard in the fabrication of submicrometer transistors. Furthermore, the materials used in many of the first generation, top-down NEMS devices, (Si, GaAs, Si_3N_4, SiC) were first used in ICs and then in MEMS. Like the first MEMS devices, the first generation NEMS structures consisted of free-standing nanomechanical beams, paddle oscillators, and tethered plates made using simple bulk and single layer surface *nano*machining processes. Recent advancements have focused on incorporating *nano*materials such as nanotubes and nanowires synthesized using bottom-up approaches into NEMS devices by integrating these materials into top-down nano- and micromachining processes. The following text serves only at a brief introduction to the technology, highlighting the key materials, fabrication approaches, and emerging application areas. For additional details and perspectives, readers are encouraged to consult an excellent review on the subject [12.58].

12.2.1 Materials and Fabrication Techniques

Like Si MEMS, Si NEMS capitalizes on well-developed processing techniques for Si and the availability of high-quality substrates. *Cleland* and *Roukes* [12.59] reported a relatively simple process to fabricate nanomechanical clamped-clamped beams directly from single-crystal (100) Si substrates. As illustrated in Fig. 12.1, the process begins with the thermal oxidation of a Si substrate (Fig. 12.1a). Large Ni contact pads were then fabricated using optical lithography and lift-off. A polymethyl methacrylate (PMMA) lift-off mold was then deposited and patterned using electron-beam lithography into the shape of nanomechanical beams (Fig. 12.1b). Ni was then deposited and patterned by lifting off the PMMA (Fig. 12.1c). Next, the underlying oxide film was patterned by RIE using the Ni film as an etch mask. After oxide etching, nanomechanical beams were patterned by etching the Si substrate using RIE, as shown in Fig. 12.1d. Following Si RIE, the Ni etch mask was removed and the sidewalls of the Si nanomechanical beams were lightly oxidized in order to protect them during the release step (Fig. 12.1e). After performing an anisotropic SiO_2 etch to clear any oxide from the field areas, the Si beams were released using an isotropic Si RIE step, as shown in Fig. 12.1f. After release, the protective SiO_2 film was removed by wet etching in HF (Fig. 12.1g). Using this process, the authors reported the successful fabrication of nanomechanical Si beams with micrometer-scale lengths ($\approx 8\,\mu m$) and submicrometer widths (330 nm) and heights (800 nm).

The advent of silicon-on-insulator (SOI) substrates with high quality, submicrometer-thick silicon top layers enables the fabrication of nanomechanical Si beams with fewer processing steps than the aforementioned technique, since the buried oxide layer makes these device structures relatively easy to pattern and release. Additionally, the buried SiO_2 layer electrically isolates the beams from the substrate. *Carr* and *Craighead* [12.60] detail a process that uses SOI substrates to fabricate submicrometer clamped-clamped mechanical beams and suspended plates with submicrometer tethers. The process, presented in Fig. 12.2, begins with the deposition of PMMA on an SOI substrate. The SOI substrate has a top Si layer that was either 50 or 200 nm in thickness. The PMMA is patterned into a metal lift-off mask by electron beam lithography (Fig. 12.2b). An Al film is then deposited and patterned by lift-off into a Si etch mask, as shown in Fig. 12.2c. The nanomechanical beams are then patterned by Si RIE and released by etching the underlying SiO_2 in a buffered hydrofluoric acid solution as shown in Fig. 12.2d,e, respectively. Using this process, nanomechanical beams that were 7–16 μm in length, 120–200 nm in width and 50 or 200 nm in thickness were successfully fabricated.

Fabrication of NEMS structures is not limited to Si. In fact, III–V compounds, such as gallium arsenide (GaAs), make particularly good NEMS materials from a fabrication perspective because thin epitaxial GaAs films can be grown on lattice-matched materials that can be used as sacrificial release layers. A collection of clamped-clamped nanomechanical GaAs beams fabricated on lattice-matched sacrificial layers having micrometer-scale lengths and submicrometer widths and thicknesses is shown in Fig. 12.3. *Tighe* et al. [12.61] reported on the fabrication of GaAs plates suspended with nanomechanical tethers. The structures were made from single-crystal GaAs films that were epitaxially grown on aluminum arsenide (AlAs) sacrificial layers. Ni etch masks were fabricated using electron beam lithography and lift-off as described previously. The GaAs films were patterned into beams using a chemically assisted ion beam etching process and released using a highly selective AlAs etchant. In a second example, *Tang* et al. [12.62] has capitalized on the ability to grow high-quality GaAs layers on ternary compounds such as $Al_xGa_{1-x}As$ to fabricate complex GaAs-based structures, such as submicrometer clamped-clamped beams from GaAs/AlGaAs quantum well heterostructures. As with the process described by *Tighe* et al. [12.61], this process exploits a lattice matched sacrificial layer, in this case $Al_{0.8}Ga_{0.2}As$, which can be selectively etched to release the heterostructure layers.

Silicon carbide and diamond NEMS structures have been developed for applications requiring a material with a higher acoustic velocity and/or a higher degree of chemical inertness than Si. Silicon carbide nanomechanical resonators have been successfully fabricated from both epitaxial 3C-SiC films grown on Si substrates [12.63] and bulk 6H-SiC substrates [12.64]. In the case of the 3C-SiC devices, the ultrathin epitaxial films were grown by atmospheric pressure chemical vapor deposition (APCVD) on (100)Si substrates. Nanomechanical beams were patterned using a metal RIE mask that was itself patterned by e-beam lithography. Reactive ion etching was performed using two NH_3-based plasma chemistries, with the first recipe performing an anisotropic SiC etch down to the Si substrate and the second performing an isotropic Si etch used to release the SiC beams. The two etches were performed sequentially, thereby eliminating a separate wet or dry release step. For the 6H-SiC structures, a suitable sacrificial layer was not available since the structures were fabricated directly on commercially available bulk wafers. To fabricate the structures, a metal etch mask was lithographically patterned by e-beam techniques on the 6H-SiC surface. The anisotropic SiC etch mentioned above was then performed, but with the substrate tilted roughly 45° with respect to the direction of the plasma using a special fixture to hold the wafer. A second such etch was performed on the substrate tilted back 90° with respect to the first etch, resulting in released beams with triangular cross sections.

Nanomechanical resonators have also been fashioned out of thin nanocrystalline diamond thin films [12.65]. In this case, the diamond films were deposited on SiO_2-coated Si substrates by microwave plasma chemical vapor deposition using CH_4 and H_2 as feedstock. The diamond films were patterned by RIE using metal masks patterned by e-beam lithography. The plasma chemistry in this case was based on CF_4 and O_2. The devices were then released in a buffered HF solution. It is noteworthy that the structures did not require a critical-point drying step after the wet chemical release, owing to the chemical inertness of the diamond surface.

NEMS structures are not restricted to those that can be made from patterned thin films using top-down techniques. In fact, carbon nanotubes (CNT) have been incorporated into NEMS devices using an approach that combines both bottom-up and top-down processing techniques. An example illustrating the promise and challenges of merging bottom-up with top-down techniques is the CNT-based electrostatic rotational actuator developed by *Fennimore* et al. [12.66]. In this example, multiwalled CNTs (MWCNT) are grown using a conventional arc discharge process, which typically produces an assortment of CNTs. The CNTs are then transferred to a suitable SiO_2 coated Si in a 1,2-dichlorobenzene suspension. An AFM or SEM is then used to select a properly positioned CNT as determined by prefabricated alignment marks on the substrate. Conventional electron-beam lithography and lift-off techniques are then used to pattern an Au film into contact/anchor pads on the two ends of the CNT, a rotor pad at its center and two counter electrodes at 90° to the anchor pads. Anchoring is accomplished by sandwiching the CNT between the Au contact and the underlying SiO_2 film. The rotor is released by simply etching the sacrificial SiO_2 layer, taking care not to completely undercut the anchors yet allowing for adequate clearance for the rotor. Under proper conditions, the outer wall of the MWCNTs could be detached from the inner walls in order to allow for free rotation of the rotor plate.

12.2.2 Transduction Techniques

Several unique approaches have been developed to actuate and sense the motion of NEMS devices. Electrostatic actuation can be used to actuate beams [12.67], tethered meshes [12.68], and paddle oscillators [12.69]. *Sekaric* et al. [12.70] has shown that low power lasers can be used to drive paddle oscillators into self-oscillation by induced thermal effects on the structures. In these examples, an optical detection scheme based on the modulation of incident laser light by a vibrating beam is used to detect the motion of the beams. *Cleland* and *Roukes* [12.59] describe a magnetomotive transduction technique that capitalizes on a time-varying Lorentz force created by an alternating current in the presence of a strong magnetic field. In this case, the nanomechanical beam is positioned in the magnetic field so that an AC current passing through the beam is transverse to the field lines. The resulting Lorentz force causes the beam to oscillate, which creates an electromotive force along the beam that can be detected as a voltage. Thus, in this method, the excitation and detection are performed electrically. In all of the above-mentioned cases, the measurements were performed in vacuum, presumably to minimize the effects of squeeze-film damping as well as mass loading due to adsorbates from the environment.

12.2.3 Application Areas

For the most part, NEMS technology is still in the initial stage of development. Technological challenges related to fabrication and packaging will require innovative solutions before such devices make a significant commercial impact. Nevertheless, NEMS devices have already been used for precision measurements [12.71] enabling researchers to probe the properties of matter on a nanoscopic level [12.72, 73]. Sensor technologies based on NEMS structures, most notably for attogram scale mass detection [12.74, 75], attonewton force detection [12.76], virus detection [12.77], and gaseous chemical detection [12.78] have emerged and will continue to mature. Without question, NEMS structures will prove to be useful platforms for a host of experiments and scientific discoveries in fields ranging from physics to biology, and with advancements in process integration and packaging, there is little doubt that NEMS technology will find its way into commercial micro/nanosystems as well.

12.3 Current Challenges and Future Trends

Although the field of MEMS has experienced significant growth over the past decade, many challenges still remain. In broad terms, these challenges can be grouped into three general categories:

1. Fabrication challenges
2. Packaging challenges
3. Application challenges.

Challenges in these areas will, in large measure, determine the commercial success of a particular MEMS device both in technical and economic terms. The following presents a brief discussion of some of these challenges as well as possible approaches to address them.

In terms of fabrication, MEMS is currently dominated by planar processing techniques which find their roots in silicon IC fabrication. The planar approach and the strong dependence on silicon worked well in the early years, since many of the processing tools and methodologies commonplace in IC fabrication could be directly utilized in the fabrication of MEMS devices. This approach lends itself to the integration of MEMS with silicon ICs. Therefore, it still is popular for various applications. However, modular process integration of micromachining with standard IC fabrication is not straightforward and represents a great challenge in terms of processing material compatibility, thermal budget requirements, etc. Furthermore, planar processing places significant geometric restrictions on device designs, especially for complex mechanical components requiring high aspect ratio three-dimensional geometries, which are certain to increase as the application areas for MEMS continue to grow. Along the same lines, new applications will likely demand materials other than silicon, which may not be compatible with the conventional microfabrication approach, posing a significant challenge if integration with silicon microelectronics is required. Microassembly technique can become an attractive solution to alleviate these issues. Multifunctional microsystems can be implemented by assembling various MEMS devices and electronic building blocks fabricated through disparate processing technologies. Microsystems on a common substrate will likely become the ultimate solution. Development of sophisticated modeling programs for device design and performance will become increasingly important as fabrication processes and device designs become more complex. In terms of NEMS, the most significant challenge is likely the integration of nano- and microfabrication techniques into a unified process, since NEMS devices are likely to consist of both nanoscale and microscale structures. Integration will be particularly challenging for nanoscale devices fabricated using a *bottom-up* approach, since no analog is found in microfabrication. Nevertheless, hybrid systems consisting of nanoscale and microscale components will become increasingly common as the field continues to expand.

Fabrication issues notwithstanding, packaging is and will continue to be a significant challenge to the implementation of MEMS. MEMS is unlike IC packaging which benefits from a high degree of standardization. MEMS devices inherently require interaction with the environment, and since each application has in some way a unique environment, standardization of packaging becomes extremely difficult. This lack of standardization tends to drive up the costs associated with packaging, making MEMS less competitive with alternative approaches. In addition, packaging tends to negate the effects of miniaturization based upon microfabrication, especially for MEMS devices requiring protection from certain environmental conditions. Moreover, packaging can cause performance degradation of MEMS devices, especially in situations where the environment exerts mechanical stresses on the package, which in turn results in a long-term device performance drift. To address many of these issues, wafer level packaging schemes that are customized to the device of interest will likely become more common. In essence, packaging of MEMS will move away from the conventional IC methods that utilize independently manufactured packages toward custom packages, which are created specifically for the device as a part of the batch fabrication process.

Without question, the increasing advancement of MEMS will open many new potential application areas to the technology. In most cases, MEMS will be one of several alternatives available for implementation. For cost sensitive applications, the trade off between technical capabilities and cost will challenge those who desire to commercialize the technology. The biggest challenge to the field will be to identify application areas that are well suited for MEMS/NEMS technology and have no serious challengers. As MEMS technology moves away from component level and more towards microsystems solutions, it is likely that such application areas will come to the fore.

References

12.1 M. Mehregany, S.F. Bart, L.S. Tavrow, J.H. Lang, S.D. Senturia: Principles in design and microfabrication of variable-capacitance side-drive motors, J. Vac. Sci. Technol. A **8**, 3614–3624 (1990)

12.2 Y.-C. Tai, R.S. Muller: IC-processed electrostatic synchronous micromotors, Sens. Actuators **20**, 49–55 (1989)

12.3 J.J. Sniegowski, S.L. Miller, G.F. LaVigne, M.S. Roders, P.J. McWhorter: Monolithic geared-mechanisms driven by a polysilicon surface-micromachined on-chip electrostatic microengine, IEEE Solid-State Sens. Actuators Workshop (1996) pp. 178–182

12.4 G.T.A. Kovacs: *Micromachined Transducer Sourcebook* (McGraw-Hill, Boston 1998)

12.5 S.D. Senturia: *Microsystem Design* (Kluwer, Dordrecht 1998)

12.6 J.E. Gragg, W.E. McCulley, W.B. Newton, C.E. Derrington: Compensation and calibration of a monolithic four terminal silicon pressure transducer, IEEE Solid-State Sens. Actuators Workshop (1984) pp. 21–27

12.7 Y. Wang, M. Esashi: A novel electrostatic servo capacitive vacuum sensor, IEEE Int. Conf. Solid-State Sens. Actuators (1997) pp. 1457–1460

12.8 W.H. Ko, Q. Wang: Touch mode capacitive pressure densors, Sens. Actuators **75**, 242–251 (1999)

12.9 D.J. Young, J. Du, C.A. Zorman, W.H. Ko: High-temperature single-crystal 3C-SiC capacitive pressure sensor, IEEE Sens. J. **4**, 464–470 (2004)

12.10 H. Kapels, R. Aigner, C. Kolle: Monolithic surface-micromachined sensor system for high pressure applications, Int. Conf. Solid-State Sens. Actuators (2001) pp. 56–59

12.11 J.M. Bustillo, R.T. Howe, R.S. Muller: Surface micromachining for microelectromechanical systems, Proc. IEEE **86**(8), 1552–1574 (1998)

12.12 J.H. Smith, S. Montague, J.J. Sniegowski, J.R. Murray, P.J. McWhorter: Embedded micromechanical devices for the monolithic integration of MEMS with CMOS, IEEE Int. Electron Dev. Meet. (1993) pp. 609–612

12.13 T.A. Core, W.K. Tsang, S.J. Sherman: Fabrication technology for an integrated surface-micromachined sensor, Solid State Technol. **36**(10), 39–40, 42, 46–47 (1993)

12.14 C. Lu, M. Lemkin, B.E. Boser: A monolithic surface micromachined accelerometer with digital output, IEEE Int. Solid-State Circuits Conf. (1995) pp. 160–161

12.15 N. Yazdi, K. Najafi: An all-silicon single-wafer fabrication technology for precision microaccelerometers, IEEE Int. Conf. Solid-State Sens. Actuators (1997) pp. 1181–1184

12.16 T.B. Gabrielson: Mechanical-thermal noise in micromachined acoustic and vibration sensors, IEEE Trans. Electron Dev. **40**(5), 903–909 (1993)

12.17 J. Chae, H. Kulah, K. Najafi: A monolithic three-axis micro-g micromachined silicon capacitive accelerometer, IEEE J. Solid-State Circuits **14**, 235–242 (2005)

12.18 M. Lemkin, M.A. Ortiz, N. Wongkomet, B.E. Boser, J.H. Smith: A 3-axis surface micromachined $\sum\Delta$ accelerometer, IEEE Int. Solid-State Circuits Conf. (1997) pp. 202–203

12.19 J. Wu, G.K. Fedder, L.R. Carley: A low-noise low-offset capacitive sensing amplifier for a 50 $\mu g/\sqrt{Hz}$ monolithic CMOS MEMS accelerometer, IEEE J. Solid-State Circuits **39**, 722–730 (2004)

12.20 W.A. Clark, R.T. Howe: Surface micromachined Z-axis vibratory rate gyroscope, IEEE Solid-State Sens. Actuators Workshop (1996) pp. 283–287

12.21 J.A. Geen, S.J. Sherman, J.F. Chang, S.R. Lewis: Single-chip surface micromachined integrated gyroscope with 50°/h Allan deviation, IEEE J. Solid-State Circuits **37**, 1860–1866 (2002)

12.22 H. Xie, G.K. Fedder: Fabrication, characterization, and analysis of a DRIE CMOS-MEMS gyroscope, IEEE Sens. J. **3**, 622–631 (2003)

12.23 T. Juneau, A.P. Pisano: Micromachined dual input axis angular rate sensor, IEEE Solid-State Sens. Actuators Workshop (1996) pp. 299–302

12.24 L.J. Hornbeck: Current status of the digital micromirror device (DMD) for projection television applications, IEEE Int. Electron Dev. Meet. (1993) pp. 381–384

12.25 R.S. Muller, K.Y. Lau: Surface-micromachined microoptical elements and systems, Proc. IEEE **86**(8), 1705–1720 (1998)

12.26 P.F. Van Kessel, L.J. Hornbeck, R.E. Meier, M.R. Douglass: A MEMS-based projection display, Proc. IEEE **86**(8), 1687–1704 (1998)

12.27 M.S. Cohen, M.F. Cina, E. Bassous, M.M. Oprysko, J.L. Speidell, F.J. Canora, M.J. DeFranza: Packaging of high density fiber/laser modules using passive alignment techniques, IEEE Trans. Compon. Hybrids Manuf. Technol. **15**, 944–954 (1992)

12.28 M.J. Wale, C. Edge: Self-aligned flip-chip assembly of photonic devices with electrical and optical connections, IEEE Trans. Compon. Hybrids Manuf. Technol. **13**, 780–786 (1990)

12.29 M.J. Daneman, N.C. Tien, O. Solgaard, K.Y. Lau, R.S. Muller: Linear vibromotor-actuated micromachined microreflector for integrated optical systems, IEEE Solid-State Sens. Actuators Workshop (1996) pp. 109–112

12.30 K.S.J. Pister, M.W. Judy, S.R. Burgett, R.S. Fearing: Microfabricated hinges, Sens. Actuators **33**(3), 249–256 (1992)

12.31 O. Solgaard, M. Daneman, N.C. Tien, A. Friedberger, R.S. Muller, K.Y. Lau: Optoelectronic packaging using silicon surface-micromachined alignment mirrors, IEEE Photon. Technol. Lett. **7**(1), 41–43 (1995)

12.32 S.S. Lee, L.S. Huang, C.J. Kim, M.C. Wu: 2 × 2 MEMS fiber optic switches with silicon sub-mount for low-cost packaging, IEEE Solid-State Sens. Actuators Workshop (1998) pp. 281–284

12.33 T. Akiyama, H. Fujita: A quantitative analysis of scratch drive actuator using Buckling motion, Tech. Dig., 8th IEEE Int. MEMS Workshop (1995) pp. 310–315

12.34 V.A. Aksyuk, F. Pardo, D.J. Bishop: Stress-induced curvature engineering in surface-micromachined devices, Proc. SPIE **3680**, 984 (1999)

12.35 D.J. Young, B.E. Boser: A micromachined variable capacitor for monolithic low-noise VCOs, IEEE Solid-State Sens. Actuators Workshop (1996) pp. 86–89

12.36 A. Dec, K. Suyama: Micromachined electromechanically tunable capacitors and their applications to RF IC's, IEEE Trans. Microw. Theory Tech. **46**, 2587–2596 (1998)

12.37 Z. Li, N.C. Tien: A high tuning-ratio silicon-micromachined variable capacitor with low driving voltage, IEEE Solid-State Sens. Actuators Workshop (2002) pp. 239–242

12.38 Z. Xiao, W. Peng, R.F. Wolffenbuttel, K.R. Farmer: Micromachined variable capacitor with wide tuning range, IEEE Solid-State Sens. Actuators Workshop (2002) pp. 346–349

12.39 J.J. Yao, S.T. Park, J. DeNatale: High tuning-ratio MEMS-based tunable capacitors for RF communications applications, IEEE Solid-State Sens. Actuators Workshop (1998) pp. 124–127

12.40 J.B. Yoon, C.T.-C. Nguyen: A high-Q tunable micromechanical capacitor with movable dielectric for RF applications, IEEE Int. Electron Dev. Meet. (2000) pp. 489–492

12.41 D.J. Young, V. Malba, J.J. Ou, A.F. Bernhardt, B.E. Boser: Monolithic high-performance three-dimensional coil inductors for wireless communication applications, IEEE Int. Electron Dev. Meet. (1997) pp. 67–70

12.42 D.J. Young, B.E. Boser, V. Malba, A.F. Bernhardt: A micromachined RF low phase noise voltage-controlled oscillator for wireless communication, Int. J. RF Microw. Comput.-Aided Eng. **11**(5), 285–300 (2001)

12.43 C.L. Chua, D.K. Fork, K.V. Schuylenbergh, J.P. Lu: Self-assembled out-of-plane high Q inductors, IEEE Solid-State Sens. Actuators Workshop (2002) pp. 372–373

12.44 J.B. Yoon, C.H. Han, E. Yoon, K. Lee, C.K. Kim: Monolithic high-Q overhang inductors fabricated on silicon and glass substrates, IEEE Int. Electron Dev. Meet. (1999) pp. 753–756

12.45 J.B. Yoon, Y. Choi, B. Kim, Y. Eo, E. Yoon: CMOS-compatible surface-micromachined suspended-spiral inductors for multi-GHz silicon RF ICs, IEEE Electron Dev. Lett. **23**, 591–593 (2002)

12.46 C.L. Goldsmith, Z. Yao, S. Eshelman, D. Dennis-ton: Performance of low-loss RF MEMS capacitive switches, IEEE Microw. Guided Wave Lett. **8**(8), 269–271 (1998)

12.47 J.J. Yao, M.F. Chang: A surface micromachined miniature switch for telecommunication applications with signal frequencies from DC up to 40 GHz, 8th Int. Conf. Solid-State Sens. Actuators (1995) pp. 384–387

12.48 P.M. Zavracky, N.E. McGruer, R.H. Morriosn, D. Potter: Microswitches and microrelays with a view toward microwave applications, Int. J. RF Microw. Comput.-Aided Eng. **9**(4), 338–347 (1999)

12.49 D. Hyman, J. Lam, B. Warneke, A. Schmitz, T.Y. Hsu, J. Brown, J. Schaffner, A. Walston, R.Y. Loo, M. Mehregany, J. Lee: Surface-micromachined RF MEMs switches on GaAs substrates, Int. J. RF Microw. Comput.-Aided Eng. **9**(4), 348–361 (1999)

12.50 J. Wang, Z. Ren, C.T.C. Nguyen: 1.156-GHz self-aligned vibrating micromechanical disk resonator, IEEE Trans. Ultrason. Ferr. Freq. Control **51**, 1607–1628 (2004)

12.51 Y. Wang, Z. Li, D.T. McCormick, N.C. Tien: A low-voltage lateral MEMS switch with high RF performance, J. Microelectromech. Syst. **13**, 902–911 (2004)

12.52 C.T.C. Nguyen, R.T. Howe: CMOS microelectromechanical resonator oscillator, IEEE Int. Electron Dev. Meet. (1993) pp. 199–202

12.53 L. Lin, R.T. Howe, A.P. Pisano: Microelectromechanical filters for signal processing, IEEE J. Microelectromech. Syst. **7**(3), 286–294 (1998)

12.54 F.D. Bannon III, J.R. Clark, C.T.C. Nguyen: High frequency micromechanical filter, IEEE J. Solid-State Circuits **35**(4), 512–526 (2000)

12.55 K. Wang, Y. Yu, A.C. Wong, C.T.C. Nguyen: VHF free-free beam high-*Q* micromechanical resonators, 12th IEEE Int. Conf. Micro Electro Mech. Syst. (1999) pp. 453–458

12.56 J.R. Clark, W.T. Hsu, C.T.C. Nguyen: High-*Q* VHF micromechanical contour-mode disk resonators, IEEE Int. Electron Dev. Meet. (2000) pp. 493–496

12.57 C.T.C. Nguyen, R.T. Howe: Quality factor control for micromechanical resonator, IEEE Int. Electron Dev. Meet. (1992) pp. 505–508

12.58 M.L. Roukes: Plenty of room, indeed, Sci. Am. **285**, 48–57 (2001)

12.59 A.N. Cleland, M.L. Roukes: Fabrication of high frequency nanometer scale mechanical resonators from bulk Si crystals, Appl. Phys. Lett. **69**, 2653–2655 (1996)

12.60 D.W. Carr, H.G. Craighead: Fabrication of nanoelectromechanical systems in single crystal silicon using silicon on insulator substrates and electron beam lithography, J. Vac. Sci. Technol. B **15**, 2760–2763 (1997)

12.61 T.S. Tighe, J.M. Worlock, M.L. Roukes: Direct thermal conductance measurements on suspended monocrystalline nanostructures, Appl. Phys. Lett. **70**, 2687–2689 (1997)

12.62 H.X. Tang, X.M.H. Huang, M.L. Roukes, M. Bichler, W. Wegsheider: Two-dimensional electron-gas actuation and transduction for GaAs nanoelectromechanical systems, Appl. Phys. Lett. **81**, 3879–3881 (2002)

12.63 Y.T. Yang, K.L. Ekinci, X.M.H. Huang, L.M. Schiavone, M.L. Roukes, C.A. Zorman, M. Mehregany: Monocrystalline silicon carbide nanoelectromechanical systems, Appl. Phys. Lett. **78**, 162–164 (2001)

12.64 X.M.H. Huang, X.L. Feng, M.K. Prakash, S. Kumar, C.A. Zorman, M. Mehregany, M.L. Roukes: Fabrication of suspended nanomechanical structures from bulk 6H-SiC substrates, Mater. Sci. Forum **457–460**, 1531–1534 (2004)

12.65 L. Sekaric, M. Zalalutdinov, S.W. Turner, A.T. Zehnder, J.M. Parpia, H.G. Craighead: Nanomechanical resonant structures as tunable passive modulators, Appl. Phys. Lett. **80**, 3617–3619 (2002)

12.66 A.M. Fennimore, T.D. Yuzvinsky, W.Q. Han, M.S. Fuhrer, J. Cummings, A. Zettl: Rotational actuators based on carbon nanotubes, Nature **424**, 408–410 (2003)

12.67 D.W. Carr, S. Evoy, L. Sekaric, H.G. Craighead, J.M. Parpia: Measurement of mechanical resonance and losses in nanometer scale silicon wires, Appl. Phys. Lett. **75**, 920–922 (1999)

12.68 D.W. Carr, L. Sekaric, H.G. Craighead: Measurement of nanomechanical resonant structures in single-crystal silicon, J. Vac. Sci. Technol. B **16**, 3821–3824 (1998)

12.69 S. Evoy, D.W. Carr, L. Sekaric, A. Olkhovets, J.M. Parpia, H.G. Craighead: Nanofabrication and electrostatic operation of single-crystal silicon paddle oscillators, J. Appl. Phys. **86**, 6072–6077 (1999)

12.70 L. Sekaric, J.M. Parpia, H.G. Craighead, T. Feygelson, B.H. Houston, J.E. Butler: Nanomechanical resonant structures in nanocrystalline diamond, Appl. Phys. Lett. **81**, 4455–4457 (2002)

12.71 A.N. Cleland, M.L. Roukes: A nanometre-scale mechanical electrometer, Nature **392**, 160–162 (1998)

12.72 K. Schwab, E.A. Henriksen, J.M. Worlock, M.L. Roukes: Measurement of the quantum of thermal conductance, Nature **404**, 974–977 (2000)
12.73 S. Evoy, A. Olkhovets, L. Sekaric, J.M. Parpia, H.G. Craighead, D.W. Carr: Temperature-dependent internal friction in silicon nanoelectromechanical systems, Appl. Phys. Lett. **77**, 2397–2399 (2000)
12.74 K.L. Ekinci, X.M.H. Huang, M.L. Roukes: Ultrasensitive nanoelectromechanical mass detection, Appl. Phys. Lett. **84**, 4469–4471 (2004)
12.75 B. Illic, H.G. Craighead, S. Krylov, W. Senaratne, C. Ober, P. Neuzil: Attogram detection using nanoelectromechanical oscillators, J. Appl. Phys. **95**, 3694–3703 (2004)
12.76 T.D. Stowe, K. Yasumura, T.W. Kenny, D. Botkin, K. Wago, D. Rugar: Attonewton force detection using ultrathin silicon cantilevers, Appl. Phys. Lett. **71**, 288–290 (1997)
12.77 B. Illic, Y. Yang, H.G. Craighead: Virus detection using nanoelectromechanical devices, Appl. Phys. Lett. **85**, 2604–2606 (2004)
12.78 H. Liu, J. Kameoka, D.A. Czaplewski, H.G. Craighead: Polymeric nanowire chemical sensor, Nano Lett. **4**, 617–675 (2004)